AGU PUBLICATIONS

JGR

Journal of Geophysical Research: Atmospheres

RESEARCH ARTICLE
10.1002/2016JD024942

Key Points:
- LES and DISCOVER-AQ flight data are compared to understand the role of turbulence on BVOC chemistry
- Turbulence-induced segregation is less important for OVOC than isoprene, but OVOC compensates for isoprene rate reductions
- Convection mixes more OVOC into the upper ABL and increases total OH reactivity

Supporting Information:
- Supporting Information S1

Correspondence to:
Y. Li,
yanglibj@umich.edu

Citation:
Li, Y., M. C. Barth, G. Chen, E. G. Patton, S.-W. Kim, A. Wisthaler, T. Mikoviny, A. Fried, R. Clark, and A. L. Steiner (2016), Large-eddy simulation of biogenic VOC chemistry during the DISCOVER-AQ 2011 campaign, *J. Geophys. Res. Atmos.*, *121*, 8083–8105, doi:10.1002/2016JD024942.

Received 12 FEB 2016
Accepted 22 JUN 2016
Accepted article online 27 JUN 2016
Published online 9 JUL 2016

Large-eddy simulation of biogenic VOC chemistry during the DISCOVER-AQ 2011 campaign

Yang Li[1], Mary C. Barth[2], Gao Chen[3], Edward G. Patton[2], Si-Wan Kim[4,5], Armin Wisthaler[6,7], Tomas Mikoviny[7,8], Alan Fried[9], Richard Clark[10], and Allison L. Steiner[1]

[1]Climate and Space Sciences and Engineering, University of Michigan, Ann Arbor, Michigan, USA, [2]National Center for Atmospheric Research, Boulder, Colorado, USA, [3]NASA Langley Research Center, Hampton, Virginia, USA, [4]Chemical Sciences Division, NOAA Earth System Research Laboratory, Boulder, Colorado, USA, [5]Cooperative Institute for Research in Environmental Sciences, University of Colorado Boulder, Boulder, Colorado, USA, [6]Institute of Ion Physics and Applied Physics, University of Innsbruck, Innsbruck, Austria, [7]Department of Chemistry, University of Oslo, Oslo, Norway, [8]Oak Ridge Associated Universities (ORAU), Oak Ridge, Tennessee, USA, [9]Institute of Arctic and Alpine Research, University of Colorado Boulder, Boulder, Colorado, USA, [10]Department of Earth Sciences, Millersville University of Pennsylvania, Millersville, Pennsylvania, USA

Abstract Biogenic volatile organic compounds (BVOCs) are oxidized quickly in the atmosphere to form oxygenated VOC (OVOC) and play crucial roles in the formation of ozone and secondary organic aerosols. We use the National Center for Atmospheric Research's large-eddy simulation model and Deriving Information on Surface Conditions from Column and Vertically Resolved Observations Relevant to Air Quality 2011 flight data to understand the role of boundary layer turbulence on the atmospheric chemistry of key BVOC species and their oxidation products. We simulate three distinct convective environments during the campaign, representing fair weather conditions (case 1: 1 July), a convective event dominated by southwesterly flow (case 2: 11 July), and a polluted event with high temperature and convection (case 3: 29 July). Isoprene segregation is greatest in the lower boundary layer under warm and convective conditions, reaching up to a 10% reduction in the isoprene-OH reaction rate. Under warm and convective conditions, the BVOC lifetimes lengthen due to increased isoprene emission, elevated initial chemical concentrations, and OH competition. Although turbulence-driven segregation has less influence on the OVOC species, convection mixes more OVOC into the upper atmospheric boundary layer (ABL) and increases the total OH reactivity. Production and loss rates of ozone above 2 km in all the three cases indicate in situ ozone formation in addition to vertical convective transport of ozone from the surface and aloft, consistent with the increased contribution of OH reactivity from OVOC. Together, these results show that total OH reactivity in the ABL increases under warmer and stronger convective conditions due to enhanced isoprene emission and the OVOC contribution to ozone formation.

1. Introduction

Large quantities of volatile organic compounds (VOCs) are emitted into the troposphere from biogenic and anthropogenic sources. Although anthropogenic VOCs dominate in megacities and urban areas [*Williams and Koppmann*, 2007], biogenic volatile organic compounds (BVOCs) contribute about 90% to the global VOC budget [*Guenther et al.*, 1995]. Even in some urban industrial environments, the importance of BVOC in atmospheric photochemical processes is comparable to anthropogenic VOC emissions [*Goldstein and Galbally*, 2007; *Martin et al.*, 2004]. When in combination with NO_x ($NO + NO_2$) and sunlight, BVOCs undergo a complex series of chemical reactions and play crucial roles in the formation of ozone (O_3) and secondary organic aerosols (SOAs) [*Atkinson*, 2000; *Hatfield and Huff Hartz*, 2011].

Oxygenated VOCs (OVOCs) are an important reactive fraction of VOC and are estimated to comprise 30–40% of the total hydroxyl radical (OH) reactivity in some urban areas [*Steiner et al.*, 2008; *Volkamer et al.*, 2010]. Airborne measurements up to 12 km during Intercontinental Chemical Transport Experiment-B found that OVOC accounted for up to 20% of the observed OH reactivity [*Mao et al.*, 2009], indicating its key role in the atmospheric chemistry at higher altitudes. OVOC derive from primary anthropogenic and biogenic emissions [*Sawyer et al.*, 2000; *Singh et al.*, 2001] or can be formed in the atmosphere through oxidation of other primary VOC [*Placet et al.*, 2000; *Singh et al.*, 2001]. For example, photochemical oxidation of primary BVOC, e.g., isoprene, leads to OVOC formation [*Karl et al.*, 2009]. Formaldehyde, acetaldehyde, and acetone are

frequently observed to be the most abundant OVOC in urban atmospheres [*Li et al*., 2010; *Seco et al*., 2007], and prior studies suggest that formaldehyde can contribute more than 20% to the total hydroperoxy (HO_2) radical [*Ren et al*., 2003] and enhance ozone formation by 4–10% [*Lei et al*., 2009].

As the most prevalent BVOC, isoprene (C_5H_8) is highly reactive with OH, O_3, and the nitrate radical (NO_3). The major primary OVOC products of isoprene include methyl vinyl ketone (MVK), methacrolein (MACR), and formaldehyde (HCHO). When reacting with OH, isoprene forms peroxy radicals ($C_5H_7O_2$):

(R1) $$C_5H_8 + OH \rightarrow C_5H_7O_2.$$

The fate of the isoprene peroxy radical depends on the availability of NO_x. In rural, urban, or suburban environments with NO_x emissions, OH can be recycled by reactions of peroxy radicals with NO, creating new oxidation products and forming O_3 [*Apel et al*., 2002]:

(R2) $$C_5H_7O_2 + NO \rightarrow HO_2 + MVK + MACR + \text{carbonyls}.$$

The oxidation processes of MVK and MACR by OH produce additional peroxy radicals ($MVKO_2$ and $MACRO_2$, respectively), which in the presence of NO_x produce secondary OVOC, typically in the form of carbonyls [*Spaulding et al*., 2003].

(R3) $$MVK \xrightarrow{+OH} MVKO_2 \xrightarrow{+NO} \text{carbonyls},$$

(R4) $$MACR \xrightarrow{+OH} MACRO_2 \xrightarrow{+NO} \text{carbonyls}.$$

Under low NO_x conditions such as remote forest environments, isoprene peroxy radicals typically react with the hydroperoxy radical (HO_2) to form the isoprene hydroxyhydroperoxide (ISOPOOH) or other peroxy radicals (RO_2) that form peroxides, thereby reducing the product yield of MACR and MVK [*Apel et al*., 2002].

(R5.1) $$C_5H_7O_2 + RO_2 \rightarrow \text{peroxides},$$

(R5.2) $$C_5H_7O_2 + HO_2 \rightarrow \text{ISOPOOH}.$$

In both high and low NO_x environments, the oxidation of isoprene produces a suite of OVOC that can exert additional control on the oxidative capacity of the atmosphere.

Discrepancies between observed and modeled concentrations of isoprene and its oxidation products are still high [*Carter*, 2007; *Guenther et al*., 2006; *Xie et al*., 2011], and this could be due to the accuracy required for multiple processes (emissions, chemistry, advection, vertical transport, or surface deposition) in regional and global models. The emission of primary OVOC is highly uncertain and limited by the lack of OVOC observations [*Forkel et al*., 2006; *Wang et al*., 2014], and uncertainty in their chemical fate is in part due to insufficient kinetic studies [*Bon et al*., 2011; *Seco et al*., 2013; *Sillman*, 1999; *Zheng et al*., 2009]. From the chemistry perspective, most VOC species in the atmosphere are removed through oxidation with hydroxyl radicals, but understanding these pathways is still challenging as models have difficulty simulating the hydroxyl radical in chemically complex environments [*Fuchs et al*., 2013]. In addition, many OVOC species with low volatilities can partition into the aerosol phase (e.g., SOA formation) and understanding of these gas-to-particle transitions with their liquid-phase and heterogeneous-phase oxidation pathways is still emerging [*Mellouki et al*., 2015; *Surratt et al*., 2010]. Boundary layer dynamics may also play an important role, as some OVOCs have longer lifetimes than primary emissions and can reside in the atmospheric boundary layer (ABL) over the course of several days, be trapped in nocturnal residual layers, and recirculated to the surface in the morning [*Forkel et al*., 2006]. Additionally, regional and global models often do not capture the complexities of boundary layer dynamics, causing a decoupling between the ABL and atmospheric layers aloft [*Forkel et al*., 2006]. A comprehensive understanding of the role of OVOC chemistry and its vertical distribution in the ABL has yet to be developed and evaluated in air quality models.

Previous studies have explored the effect of turbulence on chemistry using both models and observations. Early studies that accounted more explicitly for turbulence (e.g., second-order turbulence closure, direct numerical simulations, and large-eddy simulations (LESs)) found that many chemical reaction rates within the boundary layer were reduced in the presence of turbulence, due to negatively correlated concentrations and vertical velocities [*Krol et al*., 2000; *Molemaker and Vilà-Guerau de Arellano*, 1998; *Verver et al*., 1997]. This process has been described as the "segregation" of chemical species due to inefficient turbulent mixing.

Additional studies showed that clouds can play an important role in this segregation, with greater segregation and reaction rate reduction in clouds as simulated in LES models [*Vilà-Guerau de Arellano et al*., 2005] and observed [*Karl et al*., 2007]. Based on these studies, *Vinuesa and De Arellano* [2003] and *Butler et al*. [2008] added a parameterization representing segregation in chemical mechanisms and found improved predictions related to ozone chemistry and isoprene oxidation chemistry. *Ouwersloot et al*. [2011] found that the surface isoprene emission and the surface heating also played a role in segregation based on LES simulations in the Amazon, with a 10% reaction rate reduction for isoprene and OH with homogeneous surface emission and heating and up to 20% reduction with heterogeneous surface emissions. A recent study by *Kaser et al*. [2015] found that isoprene-OH segregation slowed reaction rates up to 30%, comparable to the proposed radical recycling mechanisms [*Lelieveld et al*., 2008]. Taken together, there are multiple studies that investigate chemistry-turbulence interactions for isoprene, yet few for OVOC. This study will broaden the scope to understand the role of OVOC chemistry under different convective environments.

A typical assumption is that longer-lived species such as OVOC are well mixed within the ABL [*Borrego and Incecik*, 2012] and chemical lifetimes are much longer than turbulent mixing time scales. However, observations highlight the vertical and spatial inhomogeneities in VOC oxidation products [*Koßmann et al*., 1996; *Velasco et al*., 2008; *Wöhrnschimmel et al*., 2006]. Aircraft data such as from the recent Deriving Information on Surface Conditions from Column and Vertically Resolved Observations Relevant to Air Quality (DISCOVER-AQ) field campaign can be used to address these questions. This mission was conducted in part to understand the distribution of key VOC species in the atmosphere and their importance for the formation of ozone in the ABL [*Crawford and Pickering*, 2014]. The first study took place in July 2011 in the Baltimore-Washington metropolitan area, followed by additional field campaigns in California's San Joaquin Valley (January–February 2013), Houston, TX (September 2013), and Denver, CO (July–August 2014) [*Crawford and Pickering*, 2014]. The locations were selected to target a suite of factors that influence regional air quality, including upwind emissions, transport, and local anthropogenic and biogenic emissions. Based on integration of satellite observations, aircraft in situ profiles, and surface site measurements, the DISCOVER-AQ campaigns are developing an understanding of the column and surface quantities of key O_3 precursors due to variations of surface emissions, atmospheric chemistry processes, and boundary layer meteorology. Additionally, they provide a unique opportunity to examine multiple vertical profiles of a wide suite of atmospheric constituents to understand ABL chemistry in polluted regions.

Observed vertical profiles from the DISCOVER-AQ campaigns can provide insight into atmospheric oxidation of biogenic and anthropogenic species and our ability to model these variations with existing models. However, the simplified vertical mixing scheme in regional air quality models (e.g., Community Multiscale Air Quality [*Baek et al*., 2011; *Xie et al*., 2011] or Weather Research and Forecasting model with Chemistry [*Grell et al*., 2005]) frequently has difficulty in simulating OVOC in the ABL, and VOC oxidation products and fine particulate matter are often underestimated in these regional and global chemical transport models as well [*Steiner et al*., 2008; *von Kuhlmann et al*., 2003]. In addition, global and regional models have difficulties in simulating convective cumulus clouds due to uncertainties in convective parameterizations [*Gianotti et al*., 2011; *Mapes et al*., 2004; *Mauritsen et al*., 2012]. With finer grid resolution and more complex turbulent closure, LES can resolve the energy-containing turbulent eddies in the ABL [*Moeng*, 1984]. Combined with an online chemistry scheme, LES can examine BVOC chemistry coupled with ABL dynamics accurately, elucidate the role of OVOC on regional chemistry, and serve as a comparison standard for global and regional chemical transport models and observations.

In this study, we utilize DISCOVER-AQ 2011 flight data from the Baltimore-Washington, D.C., urban area and the National Center for Atmospheric Research's (NCAR) LES model coupled to the NCAR chemical mechanism Model for OZone and Related chemical Tracers version 2.2 (MOZART2.2) [*Kim et al*., 2012] to simulate and understand the vertical distributions of key VOC species and their role in atmospheric composition and chemical distribution. With a more detailed chemical mechanism (52 reactants and 168 chemical reactions) than in *Ouwersloot et al*. [2011] (18 reactants and 19 chemical reactions), the LES model in this study provides an effective tool to analyze the chemistry of BVOC beyond isoprene. Three days with distinct meteorological conditions are selected to understand the role of BVOC in ozone formation within the ABL and the role of ABL dynamics in the primary and secondary oxidation of BVOC. By using the high time- and space-resolved VOC and oxidant data, we can compare the key mixing and chemical processes under similar NO_x environments (~1–2 ppbv) but different meteorological regimes. In addition, this study will fill a gap in understanding how segregation of VOC varies with temperature, humidity, and the presence of clouds.

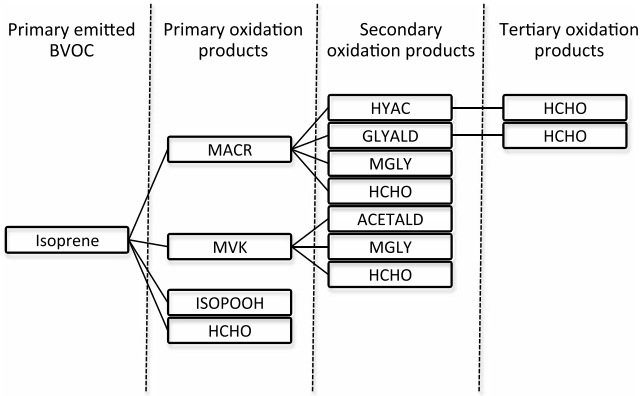

Figure 1. Chemical oxidation pathways of the biogenic volatile organic compound (BVOC) species simulated in the LES model.

2. Methods

2.1. LES Model Experiment Design

To understand the competing processes of boundary layer dynamics and chemistry, we use the NCAR LES model [*Moeng*, 1984; *Patton et al*., 2005], which solves the Navier-Stokes equations, the conservation equation for potential temperature, the Poisson equation, and the subgrid-scale kinetic energy equation for meteorological parameters. This version of the LES includes an online gas-phase chemical mechanism (NCAR MOZART2.2 [*Horowitz et al*., 2003]), as implemented and described by *Kim et al*. [2012]. This mechanism includes 52 reactants and 168 chemical reactions, and here we briefly describe the biogenic VOC and oxygenated VOC chemistry relevant to this study. MACR and MVK are the major primary OVOC products of isoprene (reactions (1) and (2)). MVK then reacts with OH (reaction (R3)) to produce acetaldehyde (CH_3CHO; ACETALD), whereas MACR oxidation (reaction (R4)) produces hydroxyacetone (CH_3COCH_2OH; HYAC), glycolaldehyde ($HOCH_2CHO$; GLYALD), and methylglyoxal (CH_3COCHO; MGLY). Under low NO_x conditions, isoprene oxidation (reaction (R5.2)) also yields hydroxyhydroperoxides ($HOCH_2COOHCH_3CHCH_2$; ISOPOOH). HCHO is formed from multiple oxidation pathways, including isoprene oxidation; MVK and MACR oxidation; and also oxidation of other secondary products, e.g., GLYALD and HYAC [*Kim et al*., 2012], and can therefore be considered both a primary-oxidation and secondary-oxidation product. The chemical pathways of these oxidation steps as represented in the LES are listed in Figure 1. For the following discussion, we categorize the VOC into (1) primary emitted BVOC (isoprene), (2) primary-oxidation products (MVK, MACR, and ISOPOOH), (3) dual-oxidation products (HCHO), and (4) secondary-oxidation products (other OVOC species, including HYAC, GLYALD, MGLY, and ACETALD).

The simulation domain is a grid with the dimensions 14.4 km × 14.4 km × 6.4 km (96 × 96 × 96 grid points resulting in horizontal grid spacing of 150 m and vertical grid spacing of 66.67 m). This resolution is coarser than that recommended by *Sullivan and Patton* [2011]; however, such a sacrifice is necessary in order to incorporate the complete MOZART2.2 mechanism. At the domain sides, periodic boundary conditions are provided in the horizontal direction with no-slip conditions at the surface, and surface stress is defined by Monin-Obukhov similarity theory as in *Kim et al*. [2012]. The aspect ratio Γ (defined as D/L, where L is the domain height and D is the horizontal width of the domain) is selected to be 2.25 to allow full turbulence development independent of the periodic sidewall boundary conditions, similar to Γ values in *Brown et al*. [2002], *Sullivan and Patton* [2011], and *van der Poel et al*. [2014].

The LES domain location is centered on the DISCOVER-AQ ground site in Fair Hill, MD (spatial scale of domain shown in Figure 2), as this is a rural site with relatively high biogenic emissions and located the greatest distance from large anthropogenic sources (e.g., Baltimore metropolitan area) among the DISCOVER-AQ ground sites. Diurnal photolysis rates are calculated with off-line NCAR Tropospheric Ultraviolet and Visible Radiation Model [*Madronich and Flocke*, 1999]. The cloud module in the LES model is included to simulate realistic cloud formation and induced convection in the cloud layer.

Three distinct weather conditions are simulated to understand the complexity of boundary layer dynamics and VOC oxidation in the ABL. The evolution of the ABL varies under different meteorological conditions, which likely affects vertical transport of BVOC. Different weather conditions may also cause changes in surface emissions of chemical species and their reaction rates, further controlling ozone formation in the atmosphere. For example, with stronger turbulence development within the ABL, longer-lived OVOC may be transported higher, causing in situ ozone production at a higher altitude. Thus, we design our simulations to span clear weather conditions to convective environments to test these hypotheses on BVOC mixing and chemical reactivity.

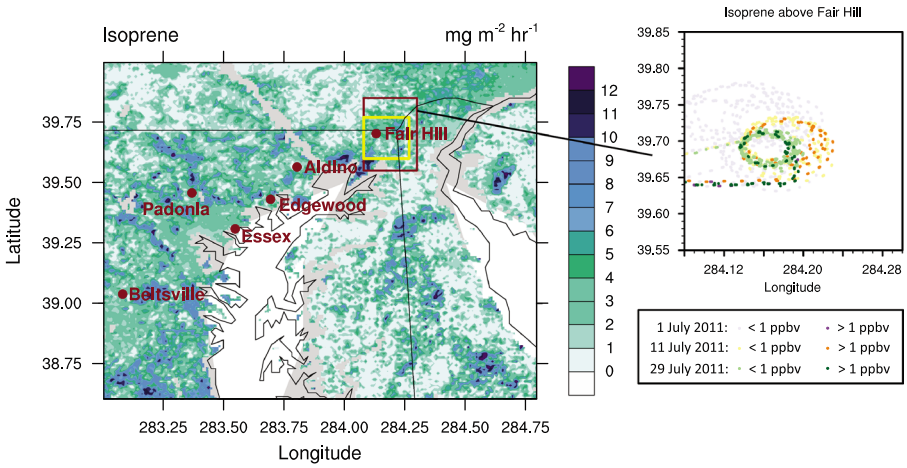

Figure 2. The spatial distribution of isoprene emission factors (mg m^{-2} h^{-1}) at standard conditions for the MEGAN canopy-scale model [*Guenther et al.*, 2006] (contour map; left) with ground-based DISCOVER-AQ sites (red dots) and the LES simulation domain (yellow box). P-3B spirals above the Fair Hill region (red box; left) are shown in the right figure, with specific measurement locations on each simulation day, with case 1 in purple (1 July 2011), case 2 in orange (11 July 2011), and case 3 in green (29 July 2011). Lighter colors represent the isoprene concentrations below 1 ppbv, and darker colors represent the isoprene concentrations above 1 ppbv.

The LES uses pseudospectral methods in the horizontal direction and a second-order finite difference method in the vertical direction for advection. A sharp wave-cutoff filter is utilized to define the resolvable-scale variables, and subgrid-scale transport is parameterized using the turbulence energy model described in *Deardorff* [1980]. Dynamics is solved using a third-order Runge-Kutta scheme with a specified Courant-Fredrichs-Lewy number, presuming that the ABL is incompressible and Boussinesq [*Sullivan and Patton*, 2011]. The full simulation time for each case is 11.5 h, starting at 05:30 LT and ending at 17:00 LT. The simulation starts at 05:30 LT with dynamics only, and when turbulent flow is established and the boundary layer dynamics have been spun up, chemical emissions and processes are then initiated at 08:30 LT [*Kim et al.*, 2012]. To understand the combined effects of boundary layer dynamics and chemistry, production and loss rates (defined as the change in mixing ratio over the change in time; ppbv s^{-1}) are calculated online in the LES for each chemical species, and the net production of individual species is calculated using Euler backward iterative solver based on production and loss rates with time step of 1.5 s [*Barth et al.*, 2003]. A bottom-up inert tracer emitted from the surface to the atmosphere is also included to calculate ABL height, which is defined as the height where the horizontally averaged mixing ratio of this scalar reaches 0.5% of its surface value [*Kim et al.*, 2012; *Vilà-Guerau de Arellano et al.*, 2005]. Passive tracers undergo the same transport processes as the reactive trace gases but do not undergo chemical transformations or dry deposition, offering a reference for chemistry versus transport processes within the ABL.

2.2. Observations

During the July 2011 DISCOVER-AQ campaign over the Baltimore-Washington metropolitan region, several flights by NASA P-3B aircraft were conducted with in situ measurements in and above the ABL (ranging from 0.3 to 5 km in height), offering more complete vertical profiles than previous observations measured by tethered balloon systems [*Andronache et al.*, 1994; *Velasco et al.*, 2008]. In addition to the flights, there were six surface measurement sites at Beltsville, Padonia, Fair Hill, Aldino, Edgewood, and Essex (ranging from 75 to 77°W and 38.5 to 40°N; Figure 2). High-time-resolution measurements on the P3-B include proton transfer reaction–mass spectrometer (PTR-MS) [*Lindinger and Jordan*, 1998] measurements of several important hydrocarbons (isoprene and monoterpenes) and a suite of oxygenated VOC (acetaldehyde, acetone, methanol, and MVK + MACR + ISOPOOH) as well as HCHO from the difference frequency generation absorption spectrometer [*Weibring et al.*, 2007]. Experimental values of MVK + MACR + ISOPOOH may be overestimated due to incomplete conversion of ISOPOOH into MVK + MACR in the inlet/instrument [*Rivera-Rios et al.*, 2014]. Surface measurements of sensible and latent heat fluxes were conducted at the Edgewood site, which is located close to Fair Hill and is the only surface location with micrometeorological measurements. Surface

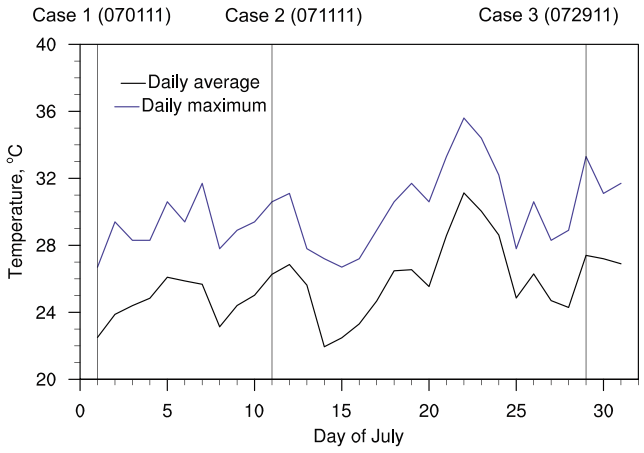

Figure 3. Daily average and maximum temperature (°C) at the Fair Hill ground site during the DISCOVER-AQ campaign. Vertical lines represent the three selected case studies: case 1 (1 July 2011; clear), case 2 (11 July 2011; convection), and case 3 (29 July 2011; high temperature and convection).

NO_x was measured using a TECO Trace Gas Analyzer by NASA Goddard Space Flight Center at the Fair Hill site during 16–31 July. Surface temperature in the Fair Hill site was measured using standard Environmental Protection Agency-approved instruments by Maryland Department of the Environment. Observational data are available through NASA DISCOVER-AQ data and information table (DISCOVER-AQ doi:10.5067/Aircraft/DISCOVER-AQ/Aerosol-TraceGas).

2.3. Case Study Selection and Model Setup

P-3B boundary layer spiral measurements were conducted on 13 days of the campaign. As shown in Figure 2, the simulation domain is located within the P-3B vertical spiral in Fair Hill. We use meteorological data from the Fair Hill ground site and DISCOVER-AQ station meteorological reports (http://discover-aq.larc.nasa.gov/planning-reports_BW2011.php) to determine weather conditions during the available observational time period and categorize days into (a) fair weather conditions (1, 2, 10, 14, and 16 July), (b) convective events (11, 20, and 22 July), and (c) polluted events with temperatures greater than 30°C (20–22 and 26–29 July). Figure 3 shows the July daily average and maximum temperatures from the Fair Hill site, and we select three of these days for model simulations to reflect different weather conditions that will likely affect VOC mixing in the ABL. Case 1 (1 July) has clear sky with moderate temperatures (daily maximum of 26.7°C) and wind speed (daytime average approximately 2 m s^{-1}); case 2 (11 July) has slightly higher temperatures (30.6°C), higher wind speeds (daytime average approximately 3 m s^{-1}), and fair weather cumulus clouds with late afternoon thunderstorms; and case 3 (29 July) has the highest daily temperature maximum (33.3°C) and moderate wind speeds (daytime average approximately 2 m s^{-1}) with afternoon cumulus clouds. Thus, case 2 and case 3 both have strong convective activity aloft leading to nonprecipitating clouds or shallow convection.

These 3 days are simulated as three separate case studies with the LES model. Meteorological boundary conditions are defined with tendencies calculated in the global 1.25° × 1.25° Modern-Era Retrospective Analysis for Research and Applications (MERRA) reanalysis [*Rienecker et al*., 2011] for 3 hourly time-averaged large-scale advective forcing and radiative tendencies. We select the MERRA grid cell covering the Fair Hill site and apply the averaged large-scale forcings for altitudes lower than 1 km, between 1 km and 2 km, and higher than 2 km (Table S1 in the supporting information). For intermediate times when reanalysis data are not available, we linearly interpolate between time steps for each of the three heights. In case 2, MERRA large-scale water vapor tendencies above 2 km enhance moisture in the domain after 09:30 LT; yet the P-3B observations indicate a persistent dry layer in the afternoon. This difference may be caused by a resolution discrepancy; e.g., the MERRA reanalysis data grid cell covers the whole Baltimore-Washington metropolitan area and represents large-scale changes, while P-3B observations represent local and more accurate conditions at the Fair Hill site. Therefore, we substitute the MERRA data above 2 km with a zero water vapor tendency to provide realistic simulation results and vertically interpolate between 1 and 2 km as in *Brown et al*. [2002].

For initial meteorological conditions, we utilize a finer resolution MERRA product (0.5° × 0.67°) for the Fair Hill location at a 6 hourly time resolution to define initial profiles of potential temperature and water vapor mixing ratio (note that tendencies were not available for this resolution product). To confirm these data with other observations, we compare the MERRA initial profiles linearly interpolated to 05:30 LT with sounding data at 08:00 LT at two locations (Wallops Island, VA (WAL: 37.93°N, 75.48°W) and Sterling, VA (IAD: 38.98°N, 77.46° W); data from http://weather.uwyo.edu/upperair/sounding.html) and P-3B observations (Figure S1 in the

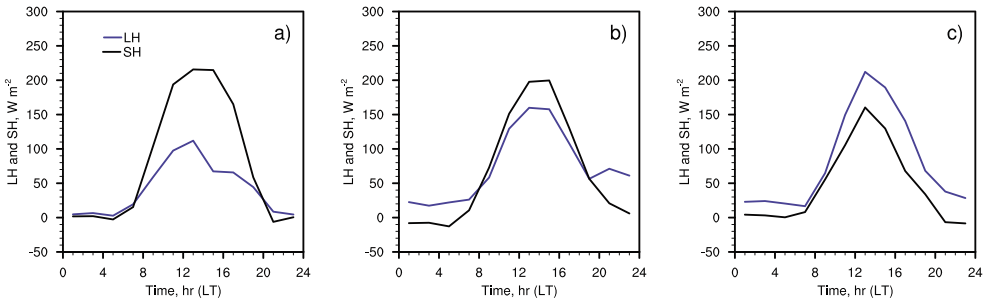

Figure 4. Observed surface sensible heat (SH; W m^{-2}; black) and latent heat (LH; W m^{-2}; blue) fluxes from the Edgewood site used as lower boundary conditions for (a) case 1, (b) case 2, and (c) case 3.

supporting information) for each simulation case. Generally, the potential temperature profiles are similar between all three data types (MERRA, soundings, and P-3B) and the LES model reproduces these profiles. For water vapor, the model initial conditions generally reproduce a realistic meteorological environment and cloud formation (Figure S1). Surface sensible and latent heat fluxes are defined from surface hourly flux measurements at the Edgewood site (Figure 2) and interpolated to the model time step. Generally, observations of wind direction from individual P-3B spirals above the Fair Hill site show a nearly constant wind direction with height (0.3–5 km), with some variations in individual cases as described below. Wind speeds average about 10 m s^{-1} (not shown) and the initial horizontal wind (u, v) is set to (10, 0) m s^{-1} at all levels in the LES.

For the model chemistry, we provide initial chemical concentrations and surface emissions (Figure 4). Initial chemical concentrations for the ABL (below 1 km) and free atmosphere (above 3 km) are based on averaged P-3B measurements above the Fair Hill site on the case study days (Table S2). CO (200 ppbv) and CH_4 (1.7 ppmv), both important sources of peroxy radicals, are assumed constant throughout the simulation with no vertical gradients and no emissions [*Kim et al*., 2012]. The initial vertical profiles of other chemical species not measured by the P-3B and the deposition velocities are the same for the three cases and prescribed as in *Kim et al*. [2012], with the initial profiles of these chemical species initialized with a photochemical box model and integrated from midnight to 08:30 LT. The photochemical box model (the Euler backward iterative method described in *Barth et al*. [2003]) has the same chemical mechanism as in the LES simulations and provides a computationally inexpensive way to study the near-surface chemistry in the absence of fluid motion.

Surface emissions of biogenic VOC (isoprene and monoterpenes) and anthropogenic NO are included in all simulations and assumed to be horizontally homogeneous over the model domain. Other anthropogenic emissions are not included. Emissions of biogenic isoprene are based on the local Model of Emissions of Gases and Aerosols from Nature (MEGAN) isoprene emission factor at standard conditions at Fair Hill (3.146 mg m^{-2} h^{-1}; Figure 2). The diurnal pattern of isoprene emission is scaled with the solar zenith angle reflecting a radiation influence as in *Kim et al*. [2012] and modified with the temperature emission activity factor according to the time-evolving temperature for each case [*Guenther et al*., 2006] (Figure 5). The temperature activity factor is defined as

$$\gamma_T = E_{\mathrm{opt}} \times \left[\frac{C_{T_2} \times e^{\left(C_{T_1} \times x\right)}}{C_{T_2} - C_{T_1} \times \left(1 - e^{\left(C_{T_2} \times x\right)}\right)} \right], \tag{1}$$

where $x = [(1/T_{\mathrm{opt}}) - (1/T)]/0.00831$, T is the temperature (K), and the empirical coefficients C_{T_1} (=95) and C_{T_2} (=230). E_{opt} and T_{opt} are estimated using equations (2) and (3).

$$T_{\mathrm{opt}} = 313 + (0.6 \times (\boldsymbol{T}_{240} - 297)), \tag{2}$$

$$E_{\mathrm{opt}} = 2.034 \times e^{(0.05 \times (T_{24} - 297))} \times e^{(0.05 \times (T_{240} - 297))}, \tag{3}$$

T_{24} and T_{240} are the average leaf temperatures over the past 24 h and 240 h [*Guenther et al*., 2006], and we define these values for each case based on hourly air temperature at the Fair Hill site. Maximum isoprene emissions are 3.15 mg m^{-2} h^{-1}, 4.11 mg m^{-2} h^{-1}, and 5.53 mg m^{-2} h^{-1} for cases 1–3, respectively. The diurnal emission of

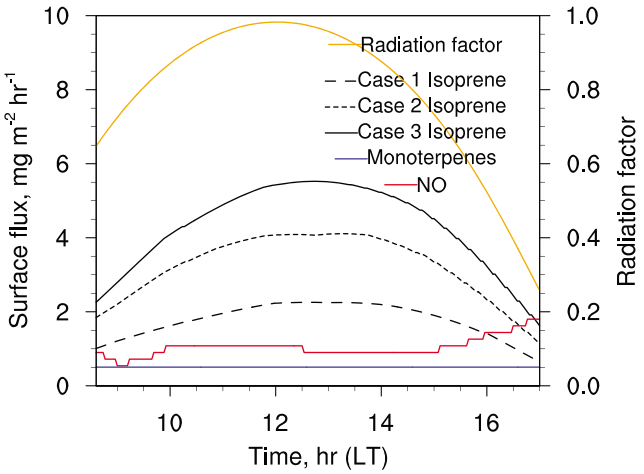

Figure 5. Diurnal surface fluxes (mg m^{-2} h^{-1}) of isoprene, NO, and monoterpenes in the LES simulations and radiation factor (unitless) for scaling isoprene emission in all the cases. Isoprene varies for each case based on changes in surface temperature, while NO and monoterpenes are the same for each simulation case.

monoterpenes for all the cases is held constant during the simulation period at a rate of 0.504 mg m^{-2} h^{-1} (Figure 5), as these emissions have a weak dependence on temperature and no dependence on light. Anthropogenic NO emissions for all cases are scaled from the observed diurnal pattern of surface NO_x observed at the ground-based sites during the campaign (16–31 July; Figure 5). Based on comparison with NO emissions from the 2011 National Emissions Inventory (http://www3.epa.gov/ttnchie1/net/2011inventory.html), this scaled NO emission from the DISCOVER-AQ observations provides a chemical environment similar to the observed condition for BVOC oxidation. In general, the three cases simulate distinct meteorological environments but similar NO_x conditions, with a maximum NO_x emission of 1.80 mg m^{-2} h^{-1} for all the cases.

2.4. Model Analysis Methods

We use instantaneous P-3B measurements from all points in space and time to evaluate the average model vertical profiles from the three simulations. While the actual time of each P-3B spiral varies depending on the flight patterns, the observed spirals typically occur from noon to early afternoon. Therefore, for comparison with P-3B data, LES-derived vertical profiles are created by averaging over the entire horizontal model domain between 11:00 and 15:00 LT. To investigate the time evolution of turbulent kinetic energy, vertical profiles of turbulent kinetic energy are created by horizontally averaging the three velocity components at an instant in time, subtracting the mean, and summing the horizontally averaged square of the velocity fluctuations. These are averaged at 2 h intervals starting at 09:00 LT to show the diurnal progression of convection within the ABL. To examine the cloud evolution, we define the cloud top at each time step as the vertical location of the maximum liquid water height across the domain and define the cloud base at each time step as the minimum liquid water height across the domain. The cloud fraction is defined as the horizontal fraction of vertically integrated liquid water. Together, these variables provide information about the variability in the ABL height.

The LES simulations are initialized by meteorological and chemical conditions derived from the observations, but there are several limitations to discuss with respect to measured-modeled comparisons. From the LES perspective, the initial or boundary meteorological condition from MERRA is limited in both space (1.25° × 1.25° for large-scale tendencies and 0.5° × 0.67° for initial θ and q profiles) and time (3 or 6 hourly depending on the product with temporal interpolation) and may not be representative of heterogeneities within the LES domain. In addition, discrepancies between simulations and observations could be affected by the lack of a detailed surface emission inventory of anthropogenic chemical species or land surface heterogeneity in the LES. From the perspective of P-3B sampling strategy, the spirals sample a single point at a time that could capture a plume from an upwind urban region or from a strong updraft with high chemical concentrations, which cannot be reproduced by the LES using homogeneous surface conditions. Despite these limitations, the evaluation of the physical and chemical processes in the LES allows us to investigate the scientific questions stated above while recognizing these sources of error.

3. Model Evaluation With Observations

We evaluate the LES simulations in this section versus data from the P3-B flights. In general, the LES simulations are idealized in that we do not represent heterogeneous surface emissions, spatial changes in the surface

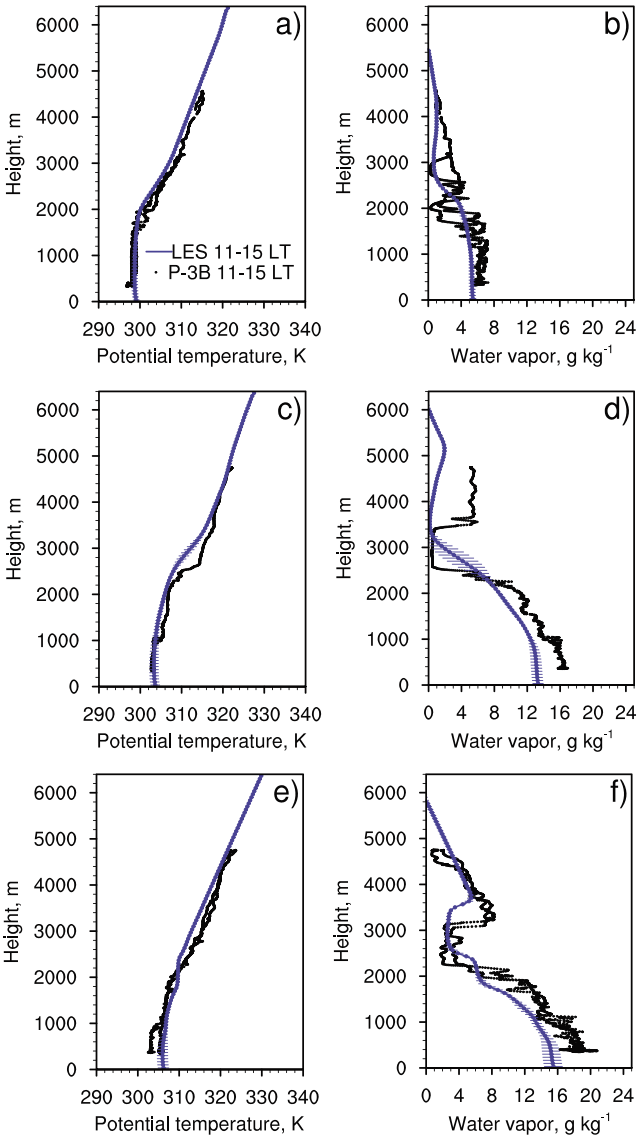

Figure 6. Comparison between P-3B observations (black dots) and domain-averaged, modeled (blue lines with horizontal bars representing the spatial standard deviation) vertical profiles of (a, c, and e) potential temperature (K) and (b, d, and f) water vapor mixing ratio (g kg^{-1}) for the three cases (case 1: Figures 6a and 6b, case 2: Figures 6c and 6d, and case 3: Figures 6e and 6f).

energy balance, or meteorologically driven changes in chemical boundary conditions. As a result, the comparison of the model with observations is not meant to be an exact representation of the observed conditions but to indicate that the model is able to reproduce the observed chemical regimes. Figure 6 compares P-3B observations and LES-simulated potential temperature (θ; K) and water vapor mixing ratio (q_v; g kg^{-1}) for the three cases. LES-simulated turbulent kinetic energy (TKE; m^2 s^{-2}) is shown at four different time periods binned in 2 h increments (Figure 7) to describe the turbulent environment, and we describe the meteorological (Figures 6 and 7) and chemical conditions (Figures 8 and 9) for each case.

3.1. Case 1: Clear-Sky, Cool Summer Day (1 July 2011)

During case 1, there is relatively clean low-level northwesterly flow with a daytime maximum temperature of 26.7°C and near-surface specific humidity of 7.98 g kg^{-1} and strong surface heating dominated by the sensible heat flux (peaking at 220 W m^{-2}; Figure 4a). The vertical profile of θ implies a neutral lower layer below 1.5 km during 11:00–15:00 LT, with a sharp inversion above (Figure 6a). LES-predicted θ is within 1° of P-3B observations in the ABL, and this discrepancy increases to about 2° above the ABL top. Observed q_v is

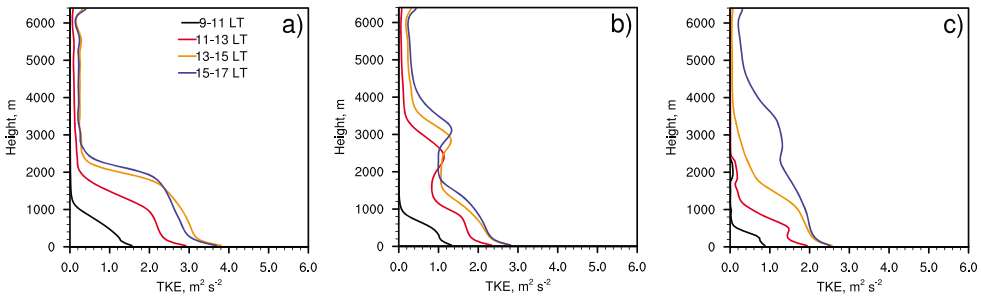

Figure 7. Domain-averaged, simulated vertical profiles of turbulent kinetic energy (m^2 s^{-2}) for (a) case 1, (b) case 2, and (c) case 3.

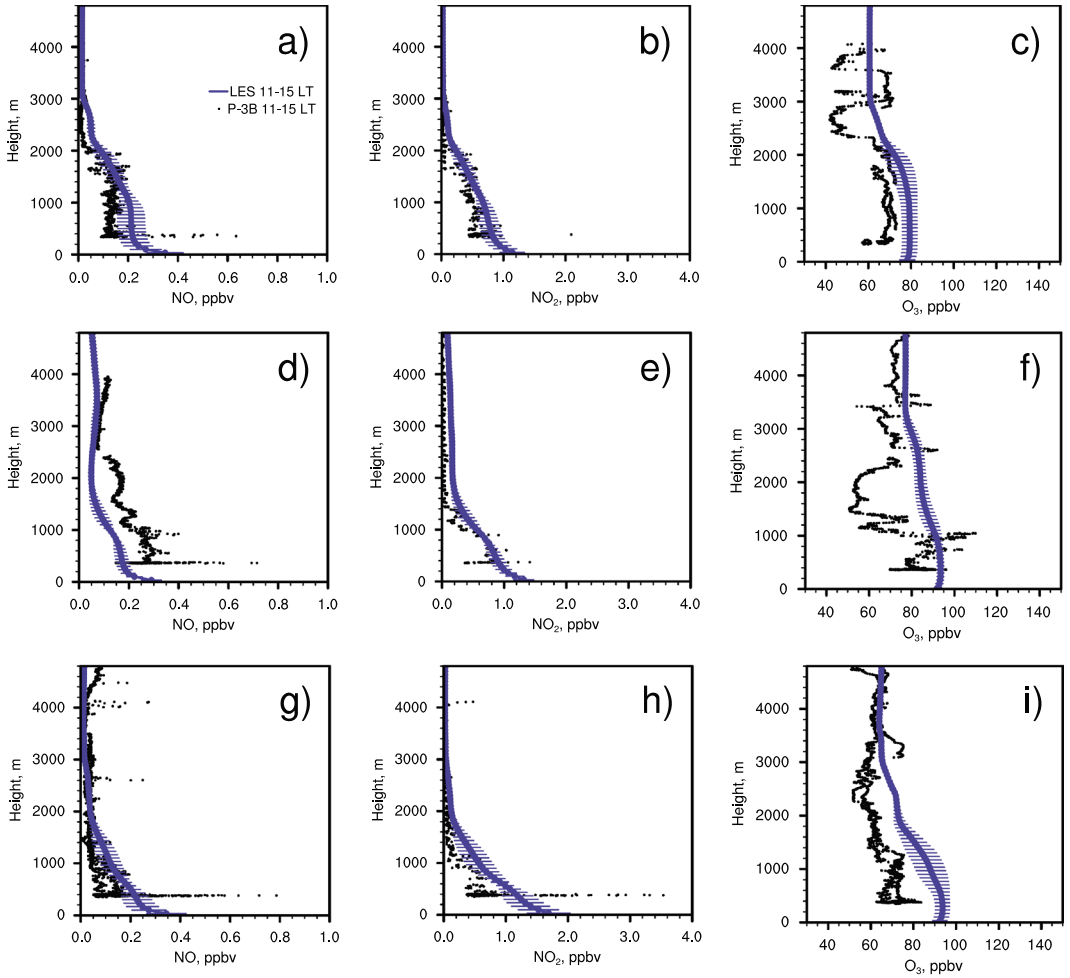

Figure 8. Comparison between P-3B observations (black dots) and domain-averaged, modeled (blue lines with horizontal bars representing the spatial standard deviation) (a, d, and g) NO (ppbv), (b, e, and h) NO_2 (ppbv), and (c, f, and i) O_3 (ppbv) during 11:00–15:00 LT for the three cases (case 1: Figures 8a–8c, case 2: Figures 8d–8f, and case 3: Figures 8g–8i).

reproduced within 3 g kg^{-1}, with the greatest variability between 1.6 km and 3 km (Figure 6b). As the day progresses, the simulated TKE increases at the surface and throughout the boundary layer, reaching up to about 3.7 m^2 s^{-2} in the afternoon (Figure 7a). This enhanced mixing indicates the ABL evolution, with the ABL top reaching about 2.5 km in the late afternoon. On this clear-day case, no cloud formation is simulated by the LES in the Fair Hill site, which is consistent with the lack of clouds observed by radar (http://www2.mmm.ucar.edu/imagearchive/) or the Aqua satellite (http://www-air.larc.nasa.gov/cgi-bin/ArcView/discover-aq.dc-2011?SATELLITE=1 with afternoon overpass).

Observed NO and NO_2 show well-mixed profiles below the ABL (approximately 0.1 and 0.5 ppb, respectively, below 2 km) except for a few higher mixing ratios (up to 0.6 ppb for NO and 2 ppb for NO_2) at 0.3 km and nonzero values aloft indicating their transport above the ABL (Figures 8a and 8b). The LES captures the vertical profiles of NO and NO_2 but with slightly higher values (biases of 0.04–0.08 ppbv for NO and 0.1–0.2 ppbv for NO_2) and larger gradients below 1 km. The bias between observed and simulated NO_x could be caused by the constant NO emissions implemented in the idealized case, which does not capture the spatial or temporal variability present in the NO_x emissions [*Follette-Cook et al.*, 2015]. Observed ozone concentrations vary by ~30 ppbv within and above the boundary layer, with concentrations of about 65 ppbv within the ABL during 11:00–15:00 LT (Figure 8c). The LES simulates this overall profile but produces higher ozone concentrations throughout the boundary layer (up to 78 ppbv), which could be induced by the overestimation of NO_x. The sharp decrease of observed ozone at 2.2–3 km is likely due to large-scale meteorological factors and could be caused by a shift in

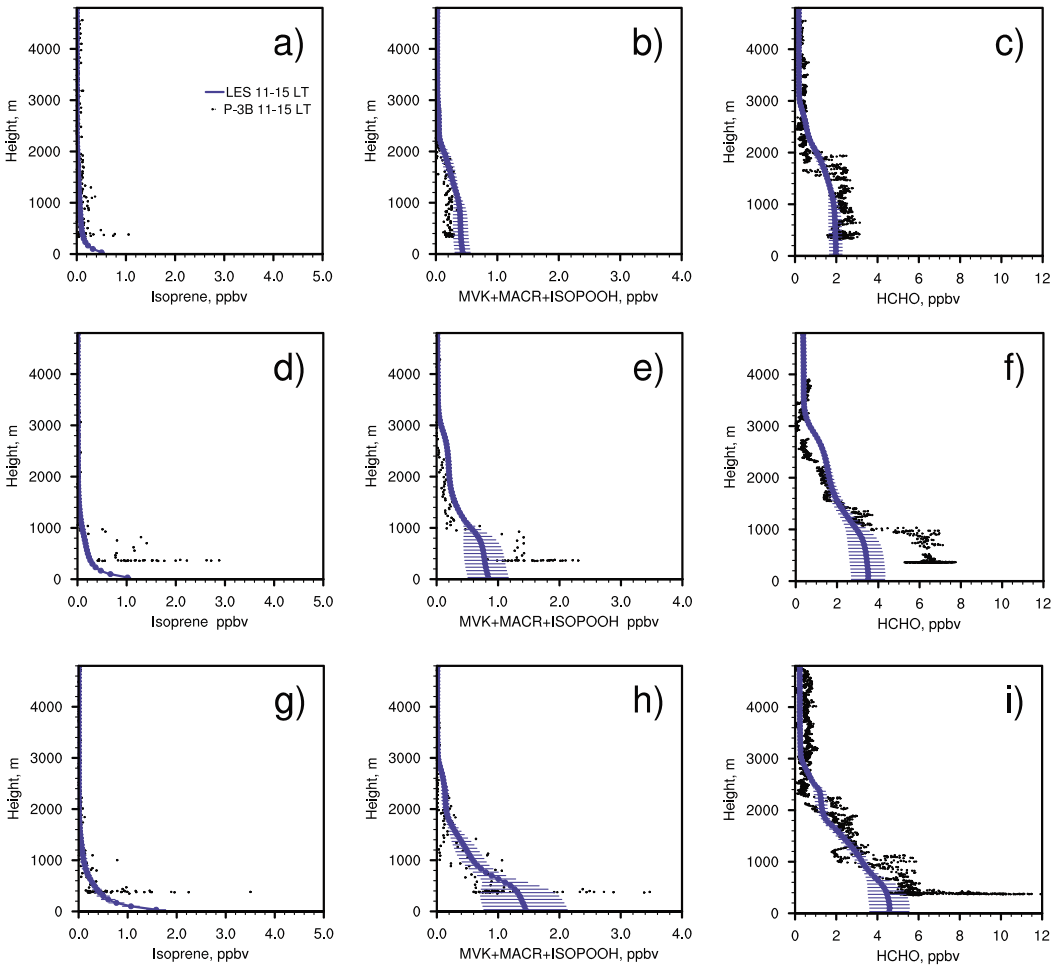

Figure 9. Comparison between P-3B observations (black dots) and domain-averaged, modeled (blue lines with horizontal bars representing the spatial standard deviation) (a, d, and g) isoprene (ppbv), (b, e, and h) MVK + MACR + ISOPOOH (ppbv), and (c, f, and i) HCHO (ppbv) during 11:00–15:00 LT for the three cases (case 1: Figures 9a–9c, case 2: Figures 9d–9f, and case 3: Figures 9g–9i).

wind direction at this time and day observed on the P-3B but not reproduced by the model. Both observed and modeled isoprene has a strong concentration gradient within the ABL, with higher concentrations near the surface that decrease above the ABL, attributed to strong surface emissions and a short chemical lifetime (Figure 9a) [*Karl et al*., 2007]. For the longer-lived VOC species, observed MVK + MACR + ISOPOOH and HCHO are well mixed within the ABL and decrease rapidly above the ABL top. The LES captures the vertical variations of isoprene and its oxidation products within 0.7 ppbv (Figures 9b and 9c).

3.2. Case 2: Moderately Warm Day With Fair Weather Cumulus Clouds (11 July 2011)

According to DISCOVER-AQ station meteorological reports (http://discover-aq.larc.nasa.gov/planning-reports_BW2011.php), case 2 is dominated by southwesterly flow around the west side of the Bermuda High. In contrast to case 1, latent heating increases up to 150 W m^{-2} at midday, accompanied by 200 W m^{-2} of sensible heat (Figure 4b). The Aqua satellite image on this day shows moderate cumulus clouds (Figure 10a). In the simulation, the daily maximum temperature peaks at 30.6°C and clouds develop at around 2 km at 11:00 LT. Clouds continue to grow to 4 km by the end of the simulation (Figure 10b), with the highest cloud fraction (37%) at around 11:30 LT (Figure 10c).

LES-predicted θ in the subcloud layer (below 2 km) is within 2° of observed values (Figure 6c). Within the cloud layer (approximately 2–4 km in the afternoon), there are larger discrepancies of both θ and q_v, with

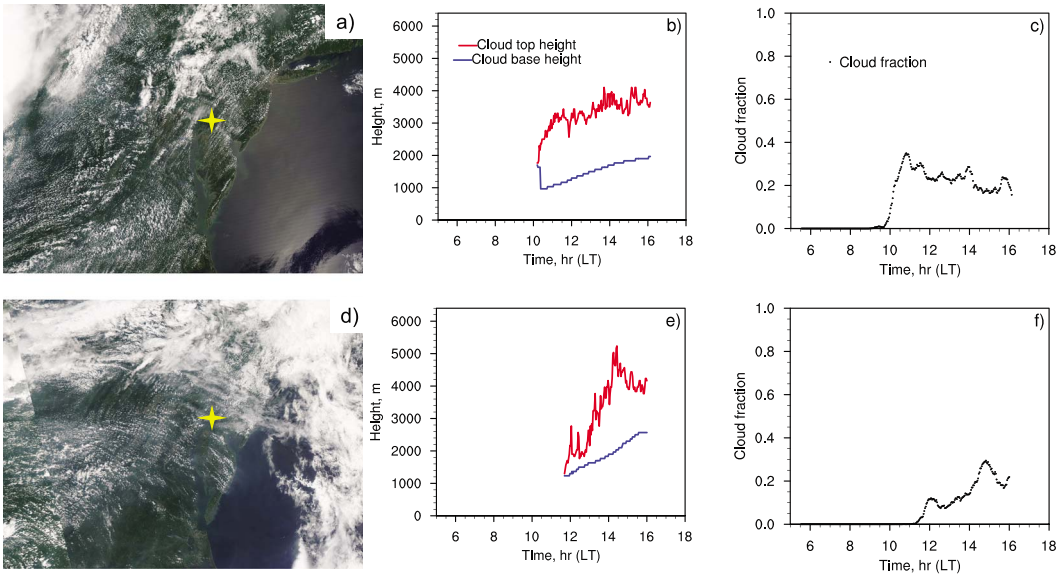

Figure 10. Aqua satellite cloud images (http://www-air.larc.nasa.gov/cgi-bin/ArcView/discover-aq.dc-2011?SATELLITE=1) with Fair Hill location noted (yellow star) for (a) case 2 and (d) case 3, temporal evolution of the cloud top and base heights (m) for (b) case 2 and (e) case 3, and the cloud fraction (unitless) for (c) case 2 and (f) case 3. Cloud top, base, and fraction are defined in section 2.4.

observed q_v about 4 g kg^{-1} drier than simulated (Figure 6d). The difference in q_v is likely the result of both the initial profile specified in the LES (which deviates from the P-3B observations due to heterogeneity of the region covered by P-3B spirals; not shown) and the drier tendencies applied above 2 km for a realistic cloud simulation. The increase of TKE above 1 km after 11:00 LT occurs within the cloud layer, indicating the development of convection. As the afternoon progresses, this convective layer deepens (Figure 7b), accompanied by an increase in the cloud base and cloud top height (Figure 10b), while near-surface TKE is lower than that in case 1. The TKE profiles suggest that vertical mixing occurs at higher altitudes than in case 1 (about 3.8 km; Figure 7b). The evolution of TKE and clouds in case 2 indicate a 1 km increase in ABL height from the morning to the late afternoon.

Case 2 observed that NO and NO_2 concentrations are slightly higher than case 1, by about 0.1 and 0.2 ppbv, respectively (Figures 8d and 8e), which may enhance OH and HCHO concentrations. Compared with case 1, isoprene concentrations are about 2 ppbv higher near the surface (~0.3 km or the lowest observations; Figure 9d). This may be in part due to higher temperatures in case 2 (32.2°C maximum temperature compared to 29.4°C for case 1) as well as the potential advective contribution from higher source regions; e.g., locations to the southwest of the Fair Hill flight path have higher emission factors in the MEGAN inventory (Figure 2). Under southwesterly winds, other chemical species are also likely transported from upwind urban areas, such as Baltimore or Washington, D.C. These relatively higher levels of precursors could contribute to the enhancement in observed O_3 compared to case 1, with observed concentrations peaking at around 93 ppbv just below the cloud base (Figure 8f). The overall O_3 profile is reproduced by the LES although lacks the observed O_3 vertical variation, which is likely due to spatial heterogeneity in ozone formation and the spiral sampling strategy. The 3-D P-3B spirals for each day (http://www-air.larc.nasa.gov/cgi-bin/ArcView/discover-aq.dc-2011?ANALYSIS=1; not shown) show O_3 hot spots in the horizontal dimension, mostly in the southwestern section of the LES model domain, which cannot be captured by LES simulations which use horizontally homogeneous surface emissions and fluxes. In addition, the variability in the observed O_3 vertical structure could be affected by large-scale meteorology and changes in wind direction. During this case at this time, the wind direction shifted from a SSW wind carrying polluted air from urban areas cities to a WSW wind with cleaner air. As noted above, the LES cannot capture these chemistry-meteorology interactions as we use constant chemical boundary conditions.

In case 2, the secondary VOC products are fairly well mixed within the ABL (e.g., lower than ~1 km) and decrease sharply within the cloud layer. Observed MVK + MACR + ISOPOOH and HCHO are about 3 times greater than case 1 (Figures 9e and 9f), as reflected in the difference in the precursor isoprene (Figure 9d).

MVK + MACR + ISOPOOH and HCHO are generally underestimated by LES by up to 0.5 ppbv and 2.7 ppbv. While the initial chemical concentrations are from P-3B measurements, simulated isoprene emissions may be too low to maintain the observed atmospheric concentrations for both isoprene and its first-generation products MVK + MACR + ISOPOOH and HCHO.

3.3. Case 3: Hot, Humid Day With Afternoon Cumulus Clouds (29 July 2011)

Case 3 simulates a very hot (daytime maximum temperature 33.3°C) and humid day (daily-averaged q_v 16.45 g kg^{-1}) with strong convection in the late afternoon. In contrast to cases 1 and 2, latent heating dominates the daytime surface fluxes, reaching a daily maximum of 210 W m^{-2} (Figure 4c). The Aqua satellite image in case 3 shows enhanced regional cumulus cloud activity as compared to case 2 (Figure 10d). LES-predicted θ is within 3° of P-3B observations (Figure 6e). For q_v, the LES captures the dry layer at around 2.5 km but does not capture the fine structure in the vertical profile (Figure 6f), which may be due to the lack of surface flux heterogeneity in the LES simulations. Like case 2, simulated TKE builds throughout the day, and vertical profiles of TKE extend up to approximately 5 km, indicating cumulus congestus clouds aloft in the simulation (Figure 7c). Clouds begin forming in the simulation at about 12:30 LT and continue developing throughout the afternoon, with increased cloud fraction and the cloud top reaching 5 km at 16:00 LT (Figures 10e and 10f). The simulated increases in the ABL height from the morning to the afternoon are similar to those sampled by the aircraft for the three cases.

In case 3, observed NO and NO_2 reach a maximum of 0.8 ppbv and 3.6 ppbv, respectively, and are similar to concentrations in cases 1 and 2 as we do not simulate changes in NO_x emissions between cases. The LES overestimates NO and NO_2 by 0.1 ppbv and 0.4 ppbv near 0.3–1.5 km (Figures 8g and 8h). For ozone, observed concentrations throughout the ABL are around 70 ppbv and are fairly well mixed (Figure 8i). The LES overpredicts O_3 by up to 20 ppbv below 3.5 km during 11:00–15:00 LT, which could be induced by the overestimation of NO_x. The wind direction at all heights of each P-3B spiral was nearly constant during this case, and as a result, we do not see large fluctuations in the observed O_3 vertical structure.

LES captures the vertical profile of isoprene with the exception of the high observed concentrations near the surface (1–2 ppbv greater than simulated values; Figure 9g). For the oxygenated species, both model and observations exhibit large vertical gradients of MVK + MACR + ISOPOOH and HCHO from the surface to about 3 km (Figures 9h and 9i). For MVK + MACR + ISOPOOH, the model compares well with the observations, with a larger standard deviation below 0.7 km. However, the observations show high MVK + MACR + ISOPOOH concentrations around 0.3 km height (up to 3.6 ppbv). This is consistent with the observed elevated isoprene and most likely due to spatially heterogeneous isoprene emissions or local, instantaneous updrafts carrying high isoprene that are not captured in the model. For HCHO, observed concentrations are slightly higher than the simulated profiles below 1 km (Figure 9i). Both modeled and observed HCHO decrease from about 5 ppbv at the surface to 1 ppbv at the top of the boundary layer in near-linear fashion, suggesting strong near-surface production via chemical evolution of VOC emissions.

4. Discussion

As shown above, the idealized LES simulates P-3B observations and these simulations can be used to analyze the detailed chemical and ABL processes under meteorological conditions similar to those observed. Here we discuss the relative time scales of turbulent mixing versus chemistry and how this affects the overall BVOC lifetime and total OH reactivity of BVOC (section 4.1), the role of turbulence on VOC segregation (section 4.2), and these impacts on the formation of ozone (section 4.3).

4.1. BVOC Chemistry Versus ABL Mixing Time Scales

To understand the relative importance of atmospheric chemistry and ABL turbulent mixing, we compare the chemical lifetimes (τ_{CH}) of BVOC with the boundary layer turnover time (τ_T) and calculate the turbulent Damköhler number. We define the turbulent Damköhler number (Da_t) as the ratio of τ_T to τ_{CH}:

$$Da_t = \frac{\tau_T}{\tau_{CH}}, \tag{4}$$

where $Da_t < 1$ represents slow chemistry and $Da_t > 1$ represents fast chemistry [*Schumann*, 1989]. Based on photochemical box model calculations using surface chemical conditions (Figure S3), OH oxidation of

Table 1. Modeled Midday (11:00–13:00 LT) Lifetimes of Selected Chemical Species According to Their Reaction Rates With OH and Total Lifetimes (Calculated Based on Photolysis and Reaction With OH) of HCHO and MGLY at 0.3 km for the Three Cases[a]

	Lifetime (τ_{CH}, min)		
	Case 1	Case 2	Case 3
Isoprene	11.39 ± 0.17	12.26 ± 0.93	13.13 ± 1.10
MACR	32.88 ± 0.50	35.01 ± 2.70	37.27 ± 3.19
MVK	60.57 ± 0.89	65.33 ± 4.92	70.07 ± 5.83
ISOPOOH	153.55 ± 2.34	163.63 ± 12.60	174.31 ± 14.87
HCHO	115.57 ± 1.82	121.97 ± 9.55	129.22 ± 11.24
HYAC	385.22 ± 6.08	406.57 ± 31.83	430.75 ± 37.46
GLYALD	115.57 ± 1.82	121.97 ± 9.55	129.22 ± 11.24
MGLY	80.69 ± 1.12	88.64 ± 6.47	96.07 ± 7.70
ACETALD	81.29 ± 1.23	86.83 ± 6.66	92.63 ± 7.87
Parameters for lifetime calculation			
Temperature (K)	292.66 ± 0.42	296.88 ± 0.56	299.33 ± 0.73
OH (molecules cm^{-3})	1.44e + 7 ± 2.22e + 5	1.37e + 7 ± 1.04e + 6	1.30e + 7 ± 1.08e + 6
Total lifetime (τ_{CH}, min)			
HCHO	73.48	76.24	79.69
MGLY	49.63	52.65	55.55

[a]Values shown are horizontal (across the model domain) and temporal (11:00–13:00 LT) averages at 0.3 km, with ±1 standard deviation.

BVOC dominates all BVOC depletion processes during 11:00–13:00 LT. In the current LES configuration, we calculate τ_{CH} according to the gas-phase chemical reaction rates with OH [*Kim et al.*, 2012]:

$$\tau_{CH,X_i} = \frac{1}{k_{OH + X_i} \times [OH]}, \quad (5)$$

where $k_{OH + Xi}$ is the reaction rate coefficient (cm^3 $molecules^{-1}$ s^{-1}) for each reaction of species X_i with OH and [OH] is the ambient concentration of OH (molecules cm^{-3}). The near surface (0.3 km), midday average (11:00–13:00 LT) τ_{CH} for isoprene, its primary-oxidation products (MVK, MCAR, and ISOPOOH), its secondary-oxidation products (HYAC, GLYALD, MGLY, and ACETALD), and the dual-oxidation product (HCHO) for the three cases are listed in Table 1. Simulated temperature and [OH] used in these calculations are also included in Table 1. BVOC in case 2 and case 3 exhibit longer lifetimes than case 1. Under different meteorological conditions in the three cases, temperature likely plays a role on $k_{OH + Xi}$. The relationship between $k_{OH + Xi}$ and temperature varies in the chemical mechanism depending on the chemical species [*Kim et al.*, 2012]. For example, increasing temperature will enhance reaction barriers and reduce $k_{OH + Xi}$ for the species in Table 1 [*Allodi et al.*, 2008; *Kleindienst et al.*, 1982], with the absence of a temperature influence on the reaction rate coefficient for HCHO ($k_{OH + HCHO}$), GLYALD ($k_{OH + GLYALD}$), and HYAC ($k_{OH + HYAC}$). Other mechanisms, e.g., initial conditions, emissions, and atmospheric stability, could also influence τ_{CH} by controlling [OH] distributions.

The turbulence turnover time (τ_T) is calculated using the ratio of the ABL's characteristic length and velocity scales:

$$\tau_T = \frac{z_i}{w^*}, \quad (6)$$

where z_i is the ABL height (m) and w^* is the Deardorff convective velocity scale (m s^{-1}) calculated as

$$w^* = \left[\frac{g \times (SH + 0.61 \times LH) \times z_i}{\theta \times \rho \times c_p}\right]^{1/3}, \quad (7)$$

where g is the gravitational constant (9.8 m s^{-2}), SH is the surface sensible heat flux (m K s^{-1}), LH is the surface latent heat (m s^{-1} kg kg^{-1}), ρ is the air density (kg m^{-3}), and c_p is the air heat capacity (J kg^{-1} K^{-1}). τ_T varies throughout the day, ranging from around 9–18 min in the morning to 16–26 min in the afternoon as the ABL grows and responds to increased buoyancy forcing. τ_T is greatest in the late afternoon (16:00–17:00 LT) for case 3, due to the diminished total surface buoyancy forcing reducing w^* (Figure 11) and consistent with the lower near-surface TKE in case 3 (Figure 7c).

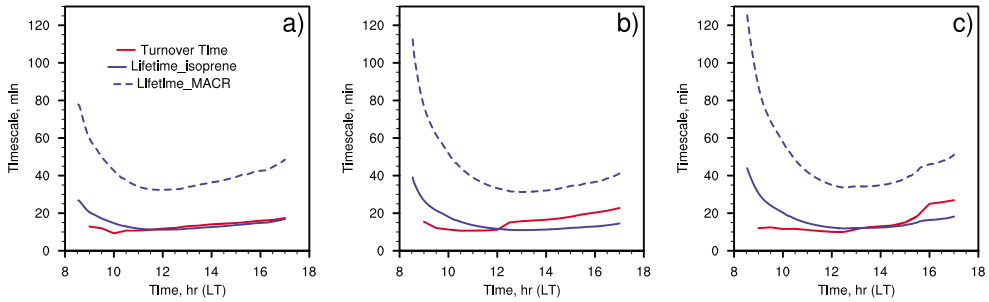

Figure 11. Comparison of diurnal turnover time (τ_T) and chemical lifetimes of isoprene ($\tau_{CH,iso}$) and MACR ($\tau_{CH,MACR}$) at 0.3 km height for (a) case 1, (b) case 2, and (c) case 3.

Da_t calculated based on the midday average (11:00–13:00 LT) τ_{CH} at 0.3 km and τ_T for the three cases (Table 2) reveals that Da_t for isoprene approaches 1 in all cases, indicating similar time scales for chemical reactivity and turbulent mixing. Da_t of MACR (0.3–0.4) is lower than isoprene but much larger than the other BVOC species. We therefore compare the diurnal variations of τ_{CH} of isoprene and MACR at 0.3 km with τ_T for the three cases (Figure 11) to examine the relationship between their OH chemistry and turbulence in detail. τ_{CH} for isoprene ($\tau_{CH,iso}$) at 0.3 km has a lifetime comparable to τ_T. Compared to τ_T, τ_{CH} is longer in the morning but decreases as the day progresses as [OH] increases at midday. These two time scales intersect roughly around noon, with some variations between the three cases. $\tau_{CH,iso}$ is the shortest in case 1, starting at approximately 20 min at the beginning of the simulation and decreasing to 10 min in the middle of the day. In cases 2 and 3, increased $\tau_{CH,iso}$ induces a later crossover point (12:00 LT in case 2 (Figure 11b) and 13:00 LT in case 3 (Figure 11c)); in these two cases, isoprene emissions are higher than case 1 due to warmer temperatures and higher initial VOC concentrations, producing increased competition for OH. Isoprene oxidation products MACR and MVK have slightly longer τ_{CH} than isoprene, but both have time scales that are of similar order of magnitude to τ_T (less than 100 min; Table 1), indicating that both turbulence and chemistry play an important role in their distribution. MACR has the shortest τ_{CH} ($\tau_{CH,MACR}$) among all the OVOC evaluated here; yet there is no crossover point in Figure 11 between $\tau_{CH,MACR}$ and τ_T. Longer $\tau_{CH,MACR}$ compared to $\tau_{CH,iso}$ indicates that MACR and OH are more well mixed than isoprene and OH. According to the contributions of different BVOC depletion processes (Figure S3), we note that the photolysis pathways of HCHO and MGLY play a comparable role to OH oxidation. Therefore, we calculate their photolysis lifetimes (Table S3) and total lifetimes (photolysis + OH reaction; Table 1). Compared with the lifetimes of HCHO and MGLY against OH in Table 1, the total lifetimes reduce 37–38% for HCHO and 37–40% for MGLY, which are closer to the turbulence turnover time scale, indicating that turbulence may have a small effect of the OH reactivity of these two species.

Table 2. Modeled Da_t of Selected Chemical Species at 0.3 km During Midday (11:00–13:00 LT) for the Three Cases[a]

	Da_t (Unitless)		
Isoprene	1.03	1.04	0.81
MACR	0.36	0.36	0.29
MVK	0.19	0.19	0.15
ISOPOOH	0.10	0.10	0.08
HCHO	0.08	0.08	0.06
HYAC	0.03	0.03	0.02
GLYALD	0.10	0.10	0.08
MGLY	0.15	0.14	0.11
ACETALD	0.14	0.15	0.11
	τ_T for Da_t calculation		
τ_T (min)	11.79 ± 0.89	12.70 ± 2.48	10.63 ± 0.62

[a] τ_T values shown are horizontal (across the model domain) and temporal (11:00–13:00 LT) averages at 0.3 km, with ±1 standard deviation. Da_t values are calculated based on these τ_T averages and the τ_{CH} averages from Table 1.

To further understand whether longer $\tau_{CH,iso}$ and $\tau_{CH,MACR}$ in cases 2 and 3 results from OH competition, OH reactivity of the BVOC species at 0.3 km, 1.5 km, and 2.7 km during midday is calculated as

$$R_{OH+X_i} = k_{OH+X_i} \times [X_i], \quad (8)$$

$$R_{BVOC} = \sum R_{OH\ +\ X_i}, \quad (9)$$

where $[X_i]$ is the ambient concentration of BVOC species i (molecules cm^{-3}) and R_{OH} is the OH reactivity (s^{-1}). Total OH reactivity of BVOC (R_{BVOC}) is the sum of the OH reactivity for all the BVOC species in Table 1 and shown in Figure 12 for three altitudes: 0.3 km to represent the near

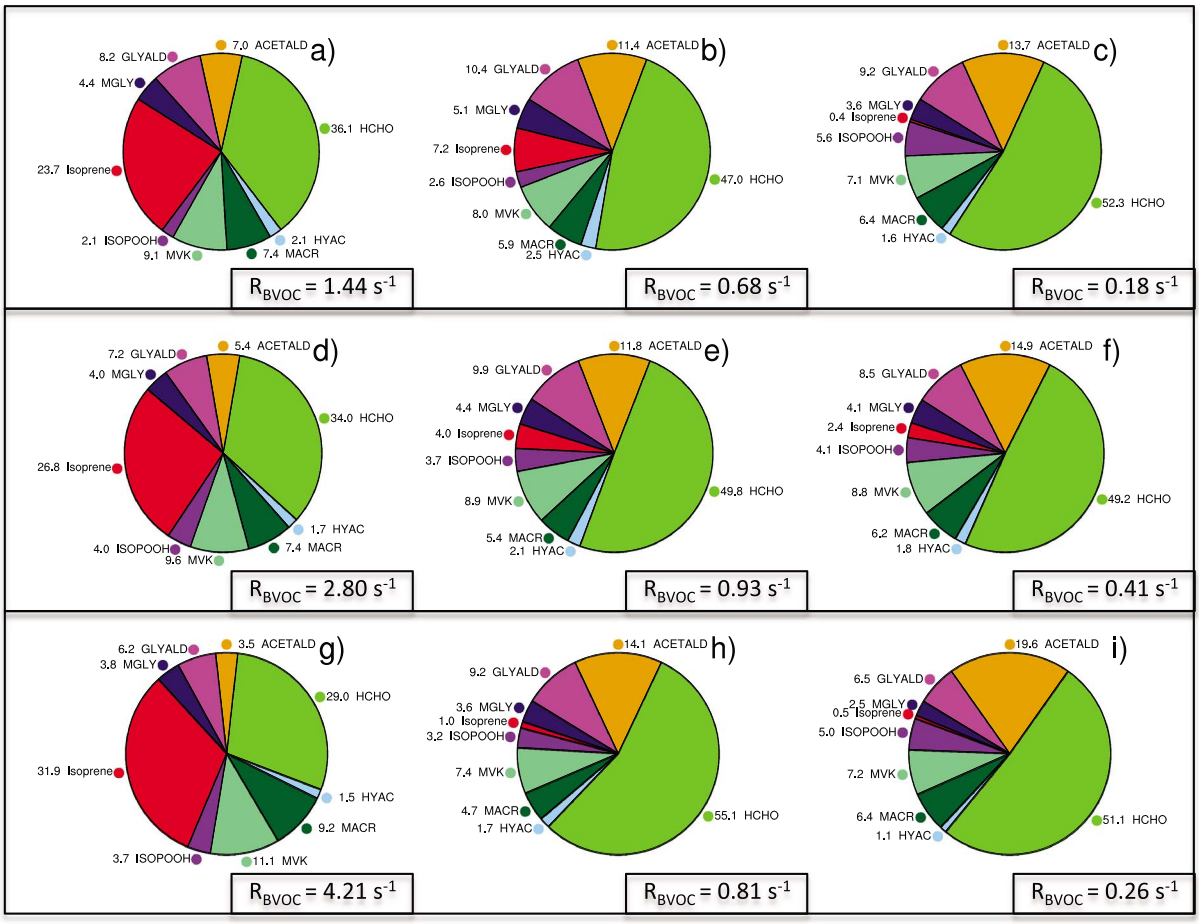

Figure 12. LES-simulated OH reactivity contribution percentages (%) and total BVOC + OH reactivity (R_{BVOC}; black box) of the BVOC species at (a, d, and g) 0.3 km, (b, e, and h) 1.5 km, and (c, f, and i) 2.7 km during midday (11:00–13:00 LT) for the three cases (case 1: Figures 12a–12c, case 2: Figures 12d–12f, and case 3: Figures 12g–12i).

surface and 1.5 km and 2.7 km to show the chemical environments around the cloud base and cloud top height at midday for case 2. In all cases, R_{BVOC} decreases with altitude from the surface to 2.7 km, consistent with the general decreasing pattern of BVOC concentrations from the surface to higher altitudes (Figure 9). At 0.3 km, R_{BVOC} increases from 1.44 s^{-1} in case 1 to 4.21 s^{-1} in case 3, due to elevated BVOC concentrations in cases 2 and 3 (Figure 12). Higher R_{BVOC} in case 2 and case 3 causes OH competition among the VOC in the ABL. In the chemical mechanism, OH is produced mainly from O_3 photolysis, followed by the reaction between HO_2 and NO. The main source of OH loss is through reactions with isoprene, followed by CO and other VOC species [*Kim et al.*, 2012]. Given the same NO emissions and CO concentrations implemented in the three cases, OH is influenced by different initial concentrations and isoprene emissions. In general, the initial concentrations of NO_x and O_3 are comparable in all the cases, while cases 2 and 3 have 1.5 to 3.5 times higher initial concentrations of VOC, respectively. In addition, isoprene emissions are the highest in case 3, followed by case 2, indicating the dominating OH depletion effects of VOC. Together, OH competition due to higher VOC concentrations decreases OH mixing ratios (Figure 13a) and increases OH loss rates (Figure 13b) at 11:00–13:00 LT in the ABL, and when combined with the temperature impact on reaction rates, this drives longer lifetimes in case 2 and case 3 (Figure 11).

Additionally, clouds play an important role in the vertical distribution of the chemical species through transport, modification of photolysis rates, and reduction of light-dependent emissions [*Kim et al.*, 2012]. We note that the current simulations do not include cloud-induced modulation of photolysis rates and isoprene emissions. Entrainment and enhanced oxidation capacity induced by clouds can increase the ratio of oxidation products with respect to isoprene [*Karl et al.*, 2007]. In case 2 at both 1.5 km and 2.7 km, higher OH reactivity is triggered by higher OVOC concentrations from earlier cloud-driven convective activity from 11:00 to 13:00

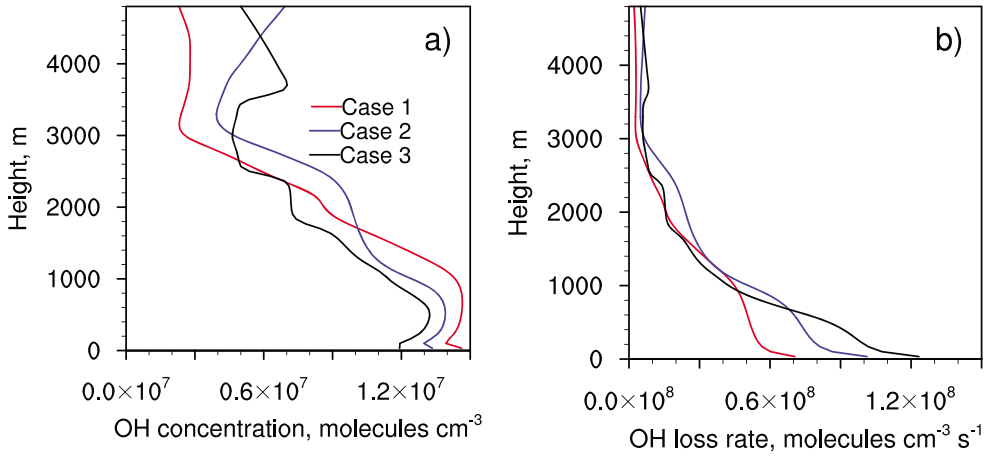

Figure 13. LES-simulated, domain-averaged (a) OH concentration and (b) loss rate during midday (11:00–13:00 LT) for the three cases.

LT [*Kim et al*., 2012; *Vilà-Guerau de Arellano et al*., 2005], while cloud formation occurs later at these two altitudes in case 3. Therefore, the influence of convection is primarily to move additional OVOC higher in the atmosphere, increasing the oxidative capacity at higher altitudes.

Individual BVOC contributions to R_{BVOC} are shown in Figure 12. Vertically, from 0.3 km (Figures 12a, 12d, and 12g) to 1.5 km (Figures 12b, 12e, and 12h) and 2.7 km (Figures 12c, 12f, and 12i), the R_{OH} contribution of isoprene (primary emission; $R_{OH + isoprene}$) decreases sharply due to near-surface chemical depletion, contributing about 25–30% at the surface to 0.5–2.5% at 2.7 km. Primary oxidation products MVK and MACR have longer chemical lifetimes than isoprene with lower near-surface contributions to total R_{OH} but similar decreasing contributions from the surface to aloft. The relatively long lifetime (>150 min) of ISOPOOH leads to little concentration variation with altitude and increased contributions to total R_{OH} aloft. In contrast, the secondary-oxidation products (ACETALD, GLYALD, MGLY, and HYAC) and HCHO show increased contributions to R_{OH} from 0.3 km to higher altitudes. For example, the increase in the ACETALD contribution can be attributed to its production from primary-oxidation products and its longer lifetime. As such, these OVOC species can be interpreted as extending the influence of the highly reactive primary VOC to regions aloft, far from the primary surface source. Increased contributions to R_{OH} from OVOC are also simulated from case 1 to case 3, consistent with the dominating convective effects over chemical consumption.

In cases 2 and 3, there are larger vertical variations in the R_{OH} contributions than in case 1. For example, the decreased percentages of primary- and early-oxidation chain species (e.g., $R_{OH + isoprene}$, $R_{OH + MVK}$, and $R_{OH + MACR}$) and the increased percentages of later oxidation chain species (e.g., $R_{OH + HCHO}$ and $R_{OH + ACETALD}$) from 0.3 km to 1.5 km are larger in case 2 and case 3 than case 1. Case 1 has larger near-surface TKE (maximum of 2.2 $m^2 s^{-2}$) below 1.5 km during 11:00–15:00 LT than case 2 (maximum of 1.8 $m^2 s^{-2}$) and case 3 (maximum of 1.5 $m^2 s^{-2}$), inducing a weaker transition of R_{OH} contributions from near surface to 1.5 km. In contrast, clouds increase convection aloft in case 2 and case 3, leading to a stronger mixing and mild gradient in R_{OH} (Figure 7). The similar distributions of R_{OH} contributions for oxidation products at 1.5 km and 2.7 km indicate their comparable reaction rates with OH reaching near steady state.

4.2. Segregation of BVOC Chemistry

A metric to further understand how boundary layer turbulence affects BVOC chemistry is the intensity of segregation (I_s) between OH and a BVOC species. We analyze segregation for isoprene (primary emission; Da_t ~1) and MACR (primary-oxidation product; Da_t ~0.35) for the three cases. I_s, described as the decreased reaction rate induced by incomplete mixing, is calculated as

$$I_s = \frac{\overline{VOC_i' \, OH'}}{\overline{VOC_i} \; \overline{OH}} , \tag{10}$$

where $\overline{VOC_i' \, OH'}$ is the horizontally averaged covariance between VOC species i and OH and $\overline{VOC_i}$ and $\overline{OH}$ are the horizontally averaged VOC and OH concentrations, respectively, while the prime in the numerator indicates

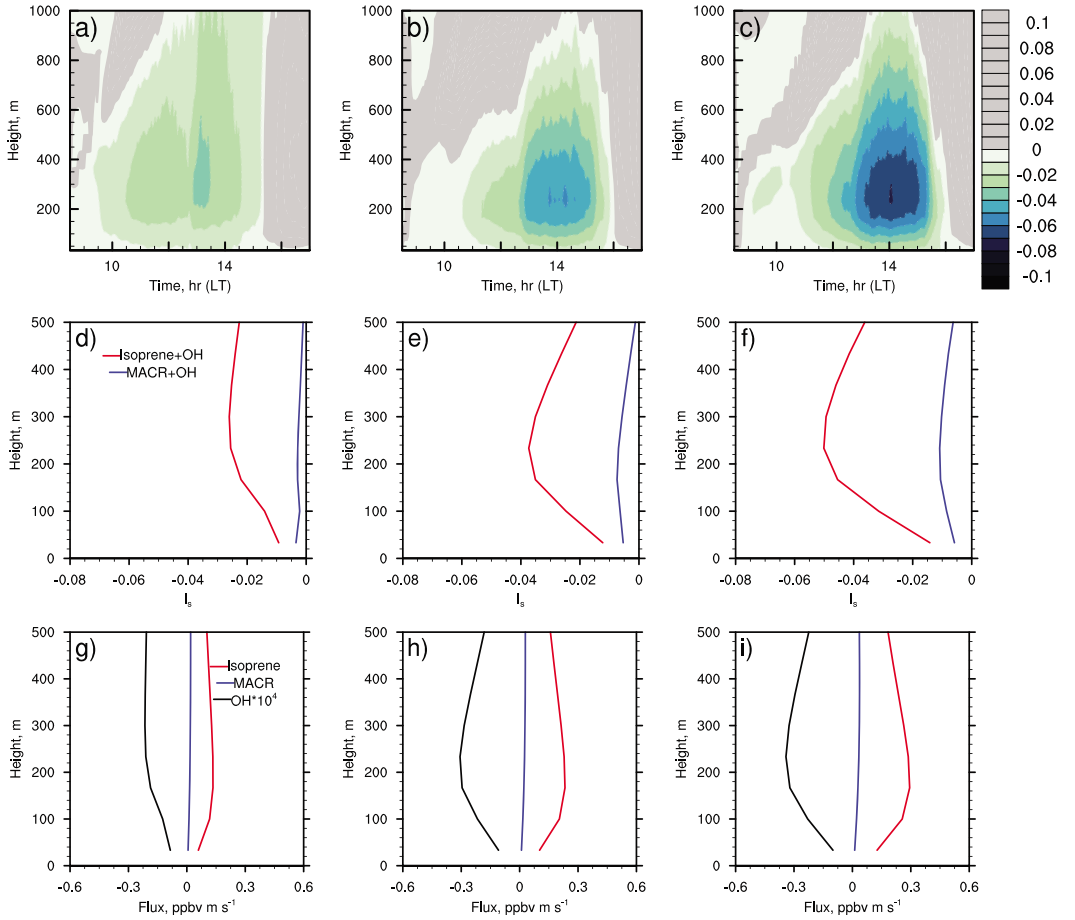

Figure 14. (a–c) LES-simulated temporal evolution of I_s for isoprene and OH; (d–f) near-surface vertical profiles of horizontal and temporal (11:00–15:00 LT) averaged I_s for isoprene and OH, MACR, and OH; and (g–i) fluxes of isoprene, MACR, and OH for the three cases (case 1: Figures 14a, 14d, and 14g; case 2: Figures 14b, 14e, and 14h; and case 3: Figures 14c, 14f, and 14i).

deviation from the horizontal average [*Karl et al.*, 2007; *Schumann*, 1989; *Sykes et al.*, 1994]. $I_s = 0$ represents the well-mixed conditions and implies zero covariance between the two species. Negative I_s indicates a decreased reaction rate due to segregation of the chemical species, with the limiting value $I_s = -1$ indicating that the two species are completely segregated, while a positive I_s represents an increased reaction rate due to similar covariance between the two reactants [*Molemaker and Vilà-Guerau de Arellano*, 1998; *Patton et al.*, 2001; *Sykes et al.*, 1994].

We calculate I_s for isoprene and OH below 1 km (Figures 14a–14c), as the BVOC reactivity is greatest near the isoprene emission source. Enhanced segregation is observed for each case between noon and early afternoon, peaking at 14:00 LT at 0.3 km altitude. Segregation increases slightly for case 2 (about −0.01 more than case 1) with the largest segregation (−0.08) in case 3. Therefore, case 3 shows the strongest turbulence-induced reduction of the isoprene-OH reaction rate. Focusing on the strong segregation regime of isoprene and OH (below 0.5 km), midday-averaged I_s (11:00–15:00 LT) of MACR and OH is compared with I_s of isoprene and OH for the three cases (Figures 14d–14f), as the Da_t of MACR-OH could also lead to segregation [*Patton et al.*, 2001]. I_s of MACR and OH is about a factor of 10 times weaker than isoprene and OH in all the cases but with a similar vertical profile shape. Increased segregation of MACR and OH in case 2 and case 3 follows the variation of isoprene under different meteorological conditions. Despite the increase in isoprene and MACR segregation near the surface, R_{BVOC} increases due to the additional reactions of OVOC with OH as shown in section 4.1. This suggests that other VOC can compensate for the segregation-induced reduction in oxidation and maintain the oxidative capacity of the ABL.

Table 3. Segregation-Modified Midday (11:00–13:00 LT) Lifetimes of Isoprene and MACR at 0.3 km for the Three Cases[a]

	Lifetime (τ_{CH}, min)		
	Case 1	Case 2	Case 3
Isoprene	11.70 ± 0.18	12.54 ± 0.87	13.57 ± 1.00
MACR	32.96 ± 0.51	35.08 ± 2.66	S37.52 ± 3.16

[a]Values shown are horizontal (across the model domain) and temporal (11:00–13:00 LT) averages at 0.3 km, with ±1 standard deviation.

These results can be further understood by evaluating isoprene, MACR, and OH vertical flux profiles in the strong segregation regime of isoprene and OH (below 0.5 km; Figures 14g–14i). Fluxes are calculated as the horizontal average of the covariance between vertical velocity w and the individual species concentration (i.e., $w'VOC_i'$). Segregation is typically associated with organized motions in the ABL turbulence. The isoprene flux is positive (away from the surface) due to its strong surface source, and the MACR flux is slightly positive yet has a near-negligible signal. As isoprene oxidation is occurring at all heights within the near-surface layer, this creates a weak MACR gradient that does not enable a strong flux away from the surface. OH fluxes are negative (or toward the surface), indicating transport downward due to formation of OH at higher altitudes within the ABL and destruction of OH via near-surface chemistry. Therefore, the lower boundary layer (<1 km) segregation for isoprene and OH is due to the fact that the downwelling motions in this region contain the majority of the OH, while isoprene emissions are largely transported upward from the surface containing relatively low OH concentrations. These motions in the lower boundary layer are shown with instantaneous vertical cross sections through the center of the domain of OH and isoprene (Figure S2). The segregation values for isoprene-OH of <10% below the convective cloud layer under homogeneous surface forcings and emissions is comparable with the other studies over temperate forests [*Dlugi et al*., 2010; *Ouwersloot et al*., 2011].

In addition to the near surface, we find large positive I_s of isoprene and OH near the top of the ABL (not shown), indicating that isoprene and OH are transported together to the free troposphere with initially very low concentrations. As shown in Figure S2, the transport motions of isoprene and OH are consistent with convection near the top of the ABL, with the hot spots of the vertical velocity w in cases 2 and 3 also indicating cloud formation. This positive correlation is consistent with the results in *Ouwersloot et al*. [2011]. While we do not have the appropriate data to determine segregation from the P3-B observations, this result suggests that subcloud segregation may decrease the reactivity of highly reactive VOC (e.g., with lifetimes equivalent of less than isoprene) by as much as 10%.

To quantify the influence of turbulence on lifetimes of isoprene and MACR, their effective τ_{CH} (τ_{eCH}) can be recalculated using the gas-phase chemical reaction rates with OH modified by segregation [*Patton et al*., 2001]:

$$\tau_{eCH,X_i} = \frac{1}{k_{OH+X_i} \times \left(1 + I_{s,OH+X_i}\right) \times [OH]}, \quad (11)$$

where $I_{s,OH+X_i}$ is the segregation intensity between OH and X_i. τ_{eCH} of isoprene and MACR for the three cases are listed in Table 3, which are also calculated during midday (11:00–13:00 LT) at 0.3 km to compare with their original lifetimes in Table 1. Lifetimes of isoprene and MACR both increase due to segregation, with larger lifetime variations in isoprene.

4.3. Vertical Distribution of Ozone Production/Loss

Here we assess the effect of turbulence on BVOC oxidation to ozone production, formation, and loss. Simulated and observed ozone concentrations are 60–80 ppbv up to approximately the top of the domain, with discrepancies likely due to those in differences in measured and modeled NO_x and VOC (Figures 8 and 9). In each case at 15:00–17:00 LT, production and loss rates are approximately 2 times higher than at 11:00–13:00 LT at 1–2.5 km (Figure 15), consistent with a stronger convective environment and increased photooxidation producing more O_3 from OVOC precursors in the afternoon. Near-surface net ozone production in case 2 is higher than case 1, providing support to the hypothesis that higher observed ozone concentrations in case 2 are in part due to transport of precursors from upwind polluted cities under southwesterly winds. Case 3 has the largest simulated near-surface net production rate (reaching up to 0.005 ppbv s^{-1}) at 11:00–13:00 LT. Ozone production and loss occurs up to 3 km in case 1, 4.5 km in case 2, and 3.6 km in case 3, similar to the maximum heights reached by TKE evolution (Figure 7). Stronger TKE in case 2 and case 3 transports ozone precursors into the convective cloud layer (Figures 8 and 9), indicating in situ ozone

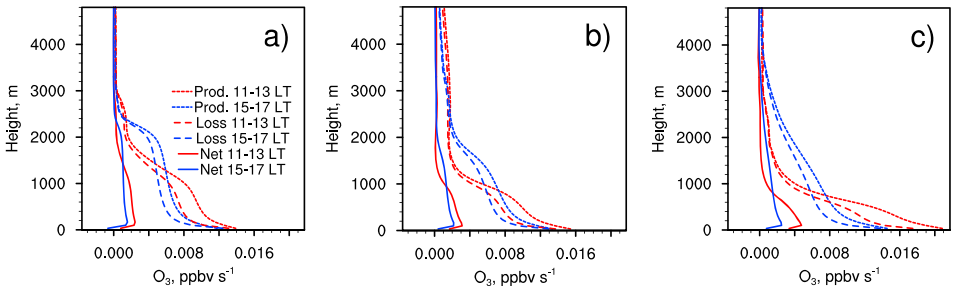

Figure 15. LES-simulated production (short dashed lines), loss (long dashed lines), and net gain (solid lines) rates of O_3 for (a) case 1, (b) case 2, and (c) case 3.

production, mostly occurring within the clouds, due to convectively transported precursors in the model (Figure 15). This in situ ozone production is an important supplement to other potential sources of ABL ozone at higher altitudes, e.g., downward mixing of ozone from the free troposphere, and long-range advection of ozone and its precursors. Enhanced ozone production rates at 0.3 km, 1.5 km, and 2.7 km during 11:00–13:00 LT in case 2 and case 3 are all consistent with the increased R_{OH} contributions described in section 4.1, with transported OVOC species dominating at the two high altitudes.

5. Conclusions

We evaluate the role of boundary layer dynamics on the atmospheric chemistry of BVOC during the DISCOVER-AQ 2011 campaign using a LES-chemistry model with well-defined turbulence. Because these eddies are highly resolved on a scale that may be relevant for fast BVOC chemistry, the LES simulations capture this relationship more accurately than coarser resolution models without coupling between turbulence and chemistry. Data analysis of the DISCOVER-AQ flights and ground-based observations provides the basis for modeling simulations. We select three cases during the campaign representing realistic meteorological conditions in the boundary layer ranging from a cool, clear-sky day to a hot, humid day with cumulus clouds. With moderate resolution in the LES model, simulated meteorological environments, including potential temperature and water vapor mixing ratio of each cases, reproduce P-3B observations in all the simulated cases. Generally, simulated concentrations of the chemical species compare well with P-3B observations.

Consistent with other studies, we find that the chemical lifetimes of highly reactive primary emissions such as isoprene are on the same scale of the boundary layer turnover time, suggesting that accurate knowledge of ABL mixing is essential for understanding the oxidation of isoprene. By evaluating BVOC segregation, we find clear diurnal and vertical variations of segregation for isoprene and OH that peak at a 10% rate reduction around 14:00 local time at 0.3 km under warm and convective environments. For the next most reactive BVOC product, MACR, the segregation is about 10 times lower than isoprene, suggesting that reactant segregation itself is not significant for most OVOC in the ABL.

While turbulence does not directly affect OVOC reaction rates, turbulent mixing affects the OVOC species in ways that alter the overall oxidative capacity of the ABL. When temperature and convection increase, we simulate longer lifetimes for the representative BVOC species in the ABL resulting from a competition for OH radicals. The effect of more vigorous turbulence on chemistry is analyzed with OH reactivity at three heights (0.3 km, 1.5 km, and 2.7 km) and the production and loss of ozone. Larger vertical variations in the OH reactivity contributions in case 2 and case 3 are consistent with the convective environments represented by the evolution of TKE. Cases 2 and 3 have higher temperatures, more water vapor, and cumulus clouds that increase transport of OVOC aloft, explaining the higher OH reactivity in these cases at 1.5 km and 2.7 km altitudes. Overall, this mixes more OVOC into the upper PBL and allows its reaction with OH, thereby increasing the oxidative capacity of the PBL. The production and loss rates of ozone follow TKE evolution, suggesting that transport of ozone precursors and in situ ozone production yield active ozone production and loss processes aloft under warm and convective environments (e.g., cases 2 and 3). Consistent with the simulated increase in BVOC lifetimes, higher concentrations of BVOC that typically occur under warmer, convective meteorological conditions lead to an increase in the total OH reactivity and an increase in OVOC contributions to the OH reactivity and ozone production aloft.

Acknowledgments
This research is supported by NASA Earth and Space Science Fellowship NNX13AN76H. The National Center for Atmospheric Research is sponsored by the National Science Foundation. We gratefully acknowledge Kenneth Davis, Chin-Hoh Moeng, and Peter Sullivan for their initiation of the study and the development of the NCAR LES model. DISCOVER-AQ 2011 campaign data are obtained through DISCOVER-AQ doi:10.5067/Aircraft/DISCOVER-AQ/Aerosol-TraceGas. The PTR-MS measurements aboard the NASA P-3B were supported by the Austrian Federal Ministry for Transport, Innovation, and Technology through the Austrian Space Applications Programme of the Austrian Research Promotion Agency. Tomas Mikoviny was supported by an appointment to the NASA Postdoctoral Program at the Langley Research Center, administered by Oak Ridge Associated Universities through a contract with NASA. We gratefully acknowledge Si-Chee Tsay (NASA Goddard Space Flight Center) for providing the NO_x measurements and Edwin Gluth (Maryland Department of the Environment) for providing the surface temperature in the Fair Hill site. MERRA IC/BC data are obtained through the Modeling and Assimilation Data and Information Services Center (http://disc.sci.gsfc.nasa.gov/daac-bin/DataHoldings.pl). For data from model runs in this paper, please contact Yang Li (University of Michigan; yanglibj@umich.edu).

References

Allodi, M. A., K. N. Kirschner, and G. C. Shields (2008), Thermodynamics of the hydroxyl radical addition to isoprene, *J. Phys. Chem. A*, *112*(30), 7064–7071.

Andronache, C., W. L. Chameides, M. O. Rodgers, J. Martinez, P. Zimmerman, and J. Greenberg (1994), Vertical distribution of isoprene in the lower boundary layer of the rural and urban southern United States, *J. Geophys. Res.*, *99*, 16,989–16,999, doi:10.1029/94JD01027.

Apel, E. C., et al. (2002), Measurement and interpretation of isoprene fluxes and isoprene, methacrolein, and methyl vinyl ketone mixing ratios at the PROPHET site during the 1998 Intensive, *J. Geophys. Res.*, *107*(D3), 4034, doi:10.1029/2000JD000225.

Atkinson, R. (2000), Atmospheric chemistry of VOCs and NO_x, *Atmos. Environ.*, *34*(12–14), 2063–2101, doi:10.1016/S1352-2310(99)00460-4.

Baek, J., Y. Hu, M. T. Odman, and A. G. Russell (2011), Modeling secondary organic aerosol in CMAQ using multigenerational oxidation of semi-volatile organic compounds, *J. Geophys. Res.*, *116*, D22204, doi:10.1029/2011JD015911.

Barth, M. C., S. Sillman, R. Hudman, M. Z. Jacobson, C. H. Kim, A. Monod, and J. Liang (2003), Summary of the cloud chemistry modeling intercomparison: Photochemical box model simulation, *J. Geophys. Res.*, *108*(D7), 4214, doi:10.1029/2002JD002673.

Bon, D. M., D. M. Bon, I. M. Ulbrich, J. A. De Gouw, and C. Warneke (2011), Measurements of volatile organic compounds at a suburban ground site (T1) in Mexico City during the MILAGRO 2006 campaign: Measurement comparison, emission ratios, and source attribution, *Atmos. Chem. Phys.*, *11*(6), 2399–2421.

Borrego, C., and S. Incecik (2012), *Air Pollution Modeling and Its Application XVI*, Springer, New York.

Brown, A. R., et al. (2002), Large-eddy simulation of the diurnal cycle of shallow cumulus convection over land, *Q. J. R. Meteorol. Soc.*, *128*(582), 1075–1093, doi:10.1256/003590002320373210.

Butler, T. M., D. Taraborrelli, C. Brühl, H. Fischer, H. Harder, M. Martinez, J. Williams, M. G. Lawrence, and J. Lelieveld (2008), Improved simulation of isoprene oxidation chemistry with the ECHAM5/MESSy chemistry-climate model: Lessons from the GABRIEL airborne field campaign, *Atmos. Chem. Phys.*, *8*(16), 4529–4546, doi:10.5194/acp-8-4529-2008.

Carter, W. P. (2007), *Development of the SAPRC-07 Chemical Mechanism and Updated Ozone Reactivity Scales*, Citeseer, Univ. Park.

Crawford, J. H., and K. E. Pickering (2014), Highlights from the Air Sensors 2014 Workshop EM: Air and Waste Management Associations Magazine for Environmental Managers, 1-47, Air & Waste Manage. Assoc., Pittsburgh, Pa.

Deardorff, J. (1980), Stratocumulus-capped mixed layers derived from a three-dimensional model, *Boundary Layer Meteorol.*, *18*(4), 495–527, doi:10.1007/BF00119502.

Dlugi, R., et al. (2010), Turbulent exchange and segregation of HO_x radicals and volatile organic compounds above a deciduous forest, *Atmos. Chem. Phys.*, *10*(13), 6215–6235, doi:10.5194/acp-10-6215-2010.

Follette-Cook, M. B., K. E. Pickering, J. H. Crawford, B. N. Duncan, C. P. Loughner, G. S. Diskin, A. Fried, and A. J. Weinheimer (2015), Spatial and temporal variability of trace gas columns derived from WRF/Chem regional model output: Planning for geostationary observations of atmospheric composition, *Atmos. Environ.*, *118*, 28–44.

Forkel, R., O. Klemm, M. Graus, B. Rappenglück, W. R. Stockwell, W. Grabmer, A. Held, A. Hansel, and R. Steinbrecher (2006), Trace gas exchange and gas phase chemistry in a Norway spruce forest: A study with a coupled 1-dimensional canopy atmospheric chemistry emission model, *Atmos. Environ.*, *40*(Supplement 1), 28–42, doi:10.1016/j.atmosenv.2005.11.070.

Fuchs, H., A. Hofzumahaus, F. Rohrer, B. Bohn, T. Brauers, H. Dorn, R. Häseler, F. Holland, M. Kaminski, and X. Li (2013), Experimental evidence for efficient hydroxyl radical regeneration in isoprene oxidation, *Nat. Geosci.*, *6*(12), 1023–1026.

Gianotti, R. L., D. Zhang, and E. A. B. Eltahir (2011), Assessment of the Regional Climate Model version 3 over the maritime continent using different cumulus parameterization and land surface schemes, *J. Clim.*, *25*(2), 638–656, doi:10.1175/JCLI-D-11-00025.1.

Goldstein, A. H., and I. E. Galbally (2007), Known and unexplored organic constituents in the Earth's atmosphere, *Environ. Sci. Technol.*, *41*(5), 1514–1521, doi:10.1021/es072476p.

Grell, G. A., S. E. Peckham, R. Schmitz, S. A. McKeen, G. Frost, W. C. Skamarock, and B. Eder (2005), Fully coupled "online" chemistry within the WRF model, *Atmos. Environ.*, *39*(37), 6957–6975, doi:10.1016/j.atmosenv.2005.04.027.

Guenther, A., et al. (1995), A global model of natural volatile organic compound emissions, *J. Geophys. Res.*, *100*, 8873–8892, doi:10.1029/94JD02950.

Guenther, A., T. Karl, P. Harley, C. Wiedinmyer, P. I. Palmer, and C. Geron (2006), Estimates of global terrestrial isoprene emissions using MEGAN (Model of Emissions of Gases and Aerosols from Nature), *Atmos. Chem. Phys.*, *6*(11), 3181–3210, doi:10.5194/acp-6-3181-2006.

Hatfield, M. L., and K. E. Huff Hartz (2011), Secondary organic aerosol from biogenic volatile organic compound mixtures, *Atmos. Environ.*, *45*(13), 2211–2219, doi:10.1016/j.atmosenv.2011.01.065.

Horowitz, L. W., et al. (2003), A global simulation of tropospheric ozone and related tracers: Description and evaluation of MOZART, version 2, *J. Geophys. Res.*, *108*(D24), 4784, doi:10.1029/2002JD002853.

Karl, T., A. Guenther, R. J. Yokelson, J. Greenberg, M. Potosnak, D. R. Blake, and P. Artaxo (2007), The tropical forest and fire emissions experiment: Emission, chemistry, and transport of biogenic volatile organic compounds in the lower atmosphere over Amazonia, *J. Geophys. Res.*, *112*, D18302, doi:10.1029/2007JD008539.

Karl, T., A. Guenther, A. Turnipseed, G. Tyndall, P. Artaxo, and S. Martin (2009), Rapid formation of isoprene photo-oxidation products observed in Amazonia, *Atmos. Chem. Phys.*, *9*(20), 7753–7767.

Kaser, L., et al. (2015), Chemistry–turbulence interactions and mesoscale variability influence the cleansing efficiency of the atmosphere, *Geophys. Res. Lett.*, *42*, 10,894–10,903, doi:10.1002/2015GL066641.

Kim, S. W., M. C. Barth, and M. Trainer (2012), Influence of fair-weather cumulus clouds on isoprene chemistry, *J. Geophys. Res.*, *117*, D10302, doi:10.1029/2011JD017099.

Kleindienst, T. E., G. W. Harris, and J. N. Pitts (1982), Rates and temperature dependences of the reaction of hydroxyl radical with isoprene, its oxidation products, and selected terpenes, *Environ. Sci. Technol.*, *16*(12), 844–846, doi:10.1021/es00106a004.

Koßmann, M., H. Vogel, B. Vogel, R. Vögtlin, U. Corsmeier, F. Fiedler, O. Klemm, and H. Schlager (1996), The composition and vertical distribution of volatile organic compounds in southwestern Germany, eastern France and northern Switzerland during the TRACT campaign in September 1992, *Phys. Chem. Earth*, *21*(5–6), 429–433, doi:10.1016/S0079-1946(97)81137-8.

Krol, M. C., M. J. Molemaker, and J. V. G. de Arellano (2000), Effects of turbulence and heterogeneous emissions on photochemically active species in the convective boundary layer, *J. Geophys. Res.*, *105*, 6871–6884, doi:10.1029/1999JD900958.

Lei, W., M. Zavala, B. De Foy, and R. Volkamer (2009), Impact of primary formaldehyde on air pollution in the Mexico City Metropolitan Area, *Atmos. Chem. Phys.*, *9*(7), 2607–2618.

Lelieveld, J., et al. (2008), Atmospheric oxidation capacity sustained by a tropical forest, *Nature*, *452*(7188), 737–740.

Li, Y., M. Shao, S. Lu, C.-C. Chang, and P. K. Dasgupta (2010), Variations and sources of ambient formaldehyde for the 2008 Beijing Olympic games, *Atmos. Environ.*, *44*(21–22), 2632–2639, doi:10.1016/j.atmosenv.2010.03.045.

Lindinger, W., and A. Jordan (1998), Proton-transfer-reaction mass spectrometry (PTR-MS): On-line monitoring of volatile organic compounds at pptv levels, *Chem. Soc. Rev.*, *27*(5), 347–375, doi:10.1039/A827347Z.

Madronich, S., and S. Flocke (1999), The role of solar radiation in atmospheric chemistry, in *Environmental Photochemistry*, edited by P. Boule, pp. 1–26, Springer, Berlin, doi:10.1007/978-3-540-69044-3_1.

Mao, J., et al. (2009), Airborne measurement of OH reactivity during INTEX-B, *Atmos. Chem. Phys.*, *9*(1), 163–173, doi:10.5194/acp-9-163-2009.

Mapes, B. E., T. T. Warner, M. Xu, and D. J. Gochis (2004), Comparison of cumulus parameterizations and entrainment using domain-mean wind divergence in a regional model, *J. Atmos. Sci.*, *61*(11), 1284–1295, doi:10.1175/1520-0469(2004)061<1284:COCPAE>2.0.CO;2.

Martin, R. V., D. D. Parrish, T. B. Ryerson, D. K. Nicks, K. Chance, T. P. Kurosu, D. J. Jacob, E. D. Sturges, A. Fried, and B. P. Wert (2004), Evaluation of GOME satellite measurements of tropospheric NO_2 and HCHO using regional data from aircraft campaigns in the southeastern United States, *J. Geophys. Res.*, *109*, D24307, doi:10.1029/2004JD004869.

Mauritsen, T., B. Stevens, E. Roeckner, T. Crueger, M. Esch, M. Giorgetta, H. Haak, J. Jungclaus, D. Klocke, and D. Matei (2012), Tuning the climate of a global model, *J. Adv. Model. Earth Syst.*, *4*, M00A01, doi:10.1029/2012MS000154.

Mellouki, A., T. J. Wallington, and J. Chen (2015), Atmospheric chemistry of oxygenated volatile organic compounds: Impacts on air quality and climate, *Chem. Rev.*, *115*(10), 3984–4014, doi:10.1021/cr500549n.

Moeng, C.-H. (1984), A large-eddy-simulation model for the study of planetary boundary-layer turbulence, *J. Atmos. Sci.*, *41*(13), 2052–2062.

Molemaker, M. J., and J. Vilà-Guerau de Arellano (1998), Control of chemical reactions by convective turbulence in the boundary layer, *J. Atmos. Sci.*, *55*(4), 568–579, doi:10.1175/1520-0469(1998)055<0568:COCRBC>2.0.CO;2.

Ouwersloot, H. G., J. Vilà-Guerau de Arellano, C. C. van Heerwaarden, L. N. Ganzeveld, M. C. Krol, and J. Lelieveld (2011), On the segregation of chemical species in a clear boundary layer over heterogeneous land surfaces, *Atmos. Chem. Phys.*, *11*(20), 10,681–10,704, doi:10.5194/acp-11-10681-2011.

Patton, E., K. Davis, M. Barth, and P. Sullivan (2001), Decaying scalars emitted by a forest canopy: A numerical study, *Boundary Layer Meteorol.*, *100*(1), 91–129, doi:10.1023/A:1019223515444.

Patton, E. G., P. P. Sullivan, and C.-H. Moeng (2005), The influence of idealized heterogeneity on wet and dry planetary boundary layers coupled to the land surface, *J. Atmos. Sci.*, *62*(7), 2078–2097, doi:10.1175/JAS3465.1.

Placet, M., C. O. Mann, R. O. Gilbert, and M. J. Niefer (2000), Emissions of ozone precursors from stationary sources: A critical review, *Atmos. Environ.*, *34*(12–14), 2183–2204, doi:10.1016/S1352-2310(99)00464-1.

Ren, X., et al. (2003), OH and HO_2 chemistry in the urban atmosphere of New York City, *Atmos. Environ.*, *37*(26), 3639–3651, doi:10.1016/S1352-2310(03)00459-X.

Rienecker, M. M., et al. (2011), MERRA: NASA's Modern-Era Retrospective Analysis for Research and Applications, *J. Clim.*, *24*(14), 3624–3648, doi:10.1175/JCLI-D-11-00015.1.

Rivera-Rios, J. C., et al. (2014), Conversion of hydroperoxides to carbonyls in field and laboratory instrumentation: Observational bias in diagnosing pristine versus anthropogenically controlled atmospheric chemistry, *Geophys. Res. Lett.*, *41*, 8645–8651, doi:10.1002/2014GL061919.

Sawyer, R. F., R. A. Harley, S. H. Cadle, J. M. Norbeck, R. Slott, and H. A. Bravo (2000), Mobile sources critical review: 1998 NARSTO assessment, *Atmos. Environ.*, *34*(12–14), 2161–2181, doi:10.1016/S1352-2310(99)00463-X.

Schumann, U. (1989), Large-eddy simulation of turbulent diffusion with chemical reactions in the convective boundary layer, *Atmos. Environ.*, *23*(8), 1713–1727, doi:10.1016/0004-6981(89)90056-5.

Seco, R., J. Peñuelas, and I. Filella (2007), Short-chain oxygenated VOCs: Emission and uptake by plants and atmospheric sources, sinks, and concentrations, *Atmos. Environ.*, *41*(12), 2477–2499, doi:10.1016/j.atmosenv.2006.11.029.

Seco, R., J. Penuelas, I. Filella, and J. Llusia (2013), Volatile organic compounds in the western Mediterranean basin: Urban and rural winter measurements during the DAURE campaign, *Atmos. Chem. Phys.*, *13*(8), 4291–4306, doi:10.5194/acp-13-4291-2013.

Sillman, S. (1999), The relation between ozone, NO_x and hydrocarbons in urban and polluted rural environments, *Atmos. Environ.*, *33*(12), 1821–1845, doi:10.1016/S1352-2310(98)00345-8.

Singh, H., Y. Chen, A. Staudt, D. Jacob, D. Blake, B. Heikes, and J. Snow (2001), Evidence from the Pacific troposphere for large global sources of oxygenated organic compounds, *Nature*, *410*(6832), 1078–1081.

Spaulding, R. S., G. W. Schade, A. H. Goldstein, and M. J. Charles (2003), Characterization of secondary atmospheric photooxidation products: Evidence for biogenic and anthropogenic sources, *J. Geophys. Res.*, *108*(D8), 4247, doi:10.1029/2002JD002478.

Steiner, A. L., A. L. Steiner, R. C. Cohen, R. A. Harley, and S. Tonse (2008), VOC reactivity in central California: Comparing an air quality model to ground-based measurements, *Atmos. Chem. Phys.*, *8*(2), 351–368, doi:10.5194/acp-8-351-2008.

Sullivan, P. P., and E. G. Patton (2011), The effect of mesh resolution on convective boundary layer statistics and structures generated by large-eddy simulation, *J. Atmos. Sci.*, *68*(10), 2395–2415, doi:10.1175/JAS-D-10-05010.1.

Surratt, J. D., A. W. H. Chan, N. C. Eddingsaas, M. Chan, C. L. Loza, A. J. Kwan, S. P. Hersey, R. C. Flagan, P. O. Wennberg, and J. H. Seinfeld (2010), Reactive intermediates revealed in secondary organic aerosol formation from isoprene, *Proc. Natl. Acad. Sci. U.S.A.*, *107*(15), 6640–6645, doi:10.1073/pnas.0911114107.

Sykes, R. I., S. F. Parker, D. S. Henn, and W. S. Lewellen (1994), Turbulent mixing with chemical reaction in the planetary boundary layer, *J. Appl. Meteorol.*, *33*(7), 825–834, doi:10.1175/1520-0450(1994)033<0825:TMWCRI>2.0.CO;2.

van der Poel, E. P., R. Ostilla-Mónico, R. Verzicco, and D. Lohse (2014), Effect of velocity boundary conditions on the heat transfer and flow topology in two-dimensional Rayleigh-B\'enard convection, *Phys. Rev. E*, *90*(1013017).

Velasco, E., C. Márquez, E. Bueno, R. Bernabé, A. Sánchez, O. Fentanes, H. Wöhrnschimmel, B. Cárdenas, A. Kamilla, and S. Wakamatsu (2008), Vertical distribution of ozone and VOCs in the low boundary layer of Mexico City, *Atmos. Chem. Phys.*, *8*(12), 3061–3079.

Verver, G. H. L., H. Van Dop, and A. A. M. Holtslag (1997), Turbulent mixing of reactive gases in the convective boundary layer, *Boundary Layer Meteorol.*, *85*(2), 197–222, doi:10.1023/A:1000414710372.

Vilà-Guerau de Arellano, J., S. W. Kim, M. C. Barth, and E. G. Patton (2005), Transport and chemical transformations influenced by shallow cumulus over land, *Atmos. Chem. Phys.*, *5*(12), 3219–3231, doi:10.5194/acp-5-3219-2005.

Vinuesa, J.-F., and J. V.-G. De Arellano (2003), Fluxes and (co-)variances of reacting scalars in the convective boundary layer, *Tellus, Ser. B*, *55*(4), 935–949, doi:10.1046/j.1435-6935.2003.00073.x.

Volkamer, R., P. Sheehy, L. T. Molina, and M. J. Molina (2010), Oxidative capacity of the Mexico City atmosphere—Part 1: A radical source perspective, *Atmos. Chem. Phys.*, *10*(14), 6969–6991, doi:10.5194/acp-10-6969-2010.

von Kuhlmann, R., M. G. Lawrence, P. J. Crutzen, and P. J. Rasch (2003), A model for studies of tropospheric ozone and nonmethane hydrocarbons: Model description and ozone results, *J. Geophys. Res.*, *108*(D9), 4294, doi:10.1029/2002JD002893.

Wang, M., M. Shao, W. Chen, B. Yuan, S. Lu, Q. Zhang, L. Zeng, and Q. Wang (2014), A temporally and spatially resolved validation of emission inventories by measurements of ambient volatile organic compounds in Beijing, China, *Atmos. Chem. Phys.*, *14*(12), 5871–5891.

Weibring, P., D. Richter, J. G. Walega, and A. Fried (2007), First demonstration of a high performance difference frequency spectrometer on airborne platforms, *Opt. Express*, *15*(21), 13,476–13,495, doi:10.1364/OE.15.013476.

Williams, J., and R. Koppmann (2007), Volatile organic compounds in the atmosphere: An overview, in *Volatile Organic Compounds in the Atmosphere*, edited by R. Koppmann, pp. 1–32, Blackwell, Oxford, U. K., doi:10.1002/9780470988657.ch1.

Wöhrnschimmel, H., C. Márquez, V. Mugica, W. A. Stahel, J. Staehelin, B. Cárdenas, and S. Blanco (2006), Vertical profiles and receptor modeling of volatile organic compounds over southeastern Mexico City, *Atmos. Environ.*, *40*(27), 5125–5136.

Xie, Y., R. Elleman, T. Jobson, and B. Lamb (2011), Evaluation of O_3-NO_x-VOC sensitivities predicted with the CMAQ photochemical model using Pacific Northwest 2001 field observations, *J. Geophys. Res.*, *116*, D20303, doi:10.1029/2011JD015801.

Zheng, J., M. Shao, W. Che, L. Zhang, L. Zhong, Y. Zhang, and D. Streets (2009), Speciated VOC emission inventory and spatial patterns of ozone formation potential in the Pearl River Delta, China, *Environ. Sci. Technol.*, *43*(22), 8580–8586, doi:10.1021/es901688e.